

Particle Physics Research Centre  
School of Physics and Astronomy  
Queen Mary University of London

## **Measurements of $H \rightarrow b\bar{b}$ decays and $VH$ production**

Thomas Charman

Supervisor: Dr. Jonathan Hays

Submitted in partial fulfillment of the requirements of the Degree of Doctor of Philosophy  
January 20, 2020.

I, Thomas Paul Charman, confirm that the research included within this thesis is my own work or that where it has been carried out in collaboration with, or supported by others, that this is duly acknowledged below and my contribution indicated. Previously published material is also acknowledged below.

I attest that I have exercised reasonable care to ensure that the work is original, and does not to the best of my knowledge break any UK law, infringe any third party's copyright or other Intellectual Property Right, or contain any confidential material.

I accept that the College has the right to use plagiarism detection software to check the electronic version of the thesis. I confirm that this thesis has not been previously submitted for the award of a degree by this or any other university.

The copyright of this thesis rests with the author and no quotation from it or information derived from it may be published without the prior written consent of the author.

Signature:

Date:

Details of collaboration and publications:

## Abstract

This report will detail the motivation for measuring the Higgs boson decaying to a pair of b quarks. First the ATLAS detector will be described in enough detail such that the capabilities and limitations of that hardware can be referred to when discussing the analysis. Then the physics theory which predicts the decay in question, the standard model of particle physics, is described including a short review of physical phenomena that are measured to exist but not included within the model. Following these elementary details the strategy for the main analysis is laid out. Due to the fact that the current iteration of this analysis is now finished details given will be those most relevant to possible future improvements of the analysis. Finally the results will be shown of work that has been completed on quantifying the uncertainty of a specific systematic error associated with the single-top background.

## Acknowledgements

- Ack 1
- Ack 2
- Ack 3

# Contents

<b>Abstract</b>	<b>3</b>
<b>Acknowledgements</b>	<b>4</b>
<b>List of Figures</b>	<b>5</b>
<b>List of Tables</b>	<b>7</b>
<b>1 Introduction</b>	<b>8</b>
<b>2 Physics Theory</b>	<b>10</b>
2.1 Historical Aside . . . . .	13
2.2 Quantum Electrodynamics . . . . .	15
2.3 Quantum Chromodynamics . . . . .	16
2.4 Electroweak theory . . . . .	17
2.5 The Brout-Englert-Higgs Mechanism . . . . .	19
2.6 Higgs bosons at the LHC . . . . .	21
<b>3 The ATLAS Detector at the Large Hadron Collider</b>	<b>23</b>
3.1 The Large Hadron Collider . . . . .	23
3.2 The ATLAS Detector . . . . .	25

<b>4 Analysis Strategy</b>	<b>35</b>
4.1 Object reconstruction . . . . .	35
4.2 Event Selection . . . . .	36
4.3 Multivariate analysis . . . . .	37
4.4 Data sets and simulation . . . . .	37
4.5 Treatment of systematic uncertainties . . . . .	38
<b>5 Results</b>	<b>40</b>
5.1 Re-weighting of single top processes . . . . .	40
<b>6 Conclusion and improvements</b>	<b>44</b>
<b>Bibliography</b>	<b>46</b>
<b>A Datasets</b>	<b>56</b>
<b>B Full Features List</b>	<b>57</b>
<b>C Theory Supplement</b>	<b>58</b>
C.1 Symmetries . . . . .	58
C.2 Gauge Bosons and the Higgs . . . . .	59
C.3 SM Lagrangian before and after spontaneous symmetry breaking . . . . .	59

# List of Figures

2.1 The Higgs potential in its fully and broken symmetric forms. . . . .	20
2.2 The four most common Higgs boson production methods from proton-proton collisions at the LHC. . . . .	21

2.3	Higgs production cross-sections (left), and branching ratios (right) for a range of centre of meass energies and Higgs boson masses respectively [1]. . . . .	22
2.4	A diagram showing a Higgs boson (decaying to a pair of b quarks) produced in association with a vector boson (decaying to 0, 1, or 2 charged leptons denoted $\ell^{+/-}$ ). . . . .	22
3.1	The CERN accelerator complex [2]. . . . .	24
3.2	Computer generated image of the whole ATLAS detector with the major sub detectors labeled [3]. . . . .	26
3.3	ATLAS magnetic field profile, showing a transverse cross-section in the centre of the detector (a), and a longitudinal section (b) [4]. . . . .	28
3.4	Computer generated image of the ATLAS inner detector [5]. . . . .	29
3.5	An image of an SCT long strip module mounted in a rig for testing at Queen Mary Univesity of London. . . . .	30
3.6	A close up image of the end of an SCT sensor in which the snake-like poly-silicon reistors are visible as a yellowish coloured structure at the end of each strip. This image was taken with a high resolution automatic area scanner commissioned by the author [6] in order to take full scans of strip sensors during the production of the ATLAS Inner Detector upgrade known as the Inner Tracker (ITk) [7, 8]. . . . .	30
3.7	Computer Generated image of the ATLAS calorimeter [9]. . . . .	32
3.8	Computer generated image of the ATLAS Muons subsystem [10]. . . . .	33
4.1	Leading order $t\bar{t}$ diagrams that also contribute to $Wt$ at next-to-leading order. . . . .	38
5.1	Plot of $\min(\Delta\phi(\ell, jet))$ in the sub-space where there are two jets that are both b-jets. . . . .	41
5.2	Plot of $m_{jj}$ in the sub-space where there are three jets and exactly two are b-jets. . . . .	42
5.3	Plot of $\Delta R(jet_1, jet_2)$ in the sub-space where there are three jets and exactly two are b-jets. . . . .	42
5.4	Plot of $p_T^{jet3}$ in the sub-space where there are three jets of which, the leading and sub-leading jets are not both b-jets (one is allowed). . . . .	43

# List of Tables

2.1	The particles of the standard model with fermions displayed on the left and bosons on the right. Quarks are in blue, leptons in red, vector bosons in yellow and scalar bosons in green. . . . .	11
5.1	The four subspaces that events were split up into before training. . . . .	41
A.1	Datasets used to train the BDT re-weighting algorithm. . . . .	56
B.1	Training variables for samples containing 2 and 3 jets. . . . .	57

# Chapter 1

## Introduction

In 2012 the Higgs boson was discovered by the ATLAS and CMS collaborations at the Large Hadron Collider [11, 12]. It was said to form the last piece of the Standard Model of Particle Physics, a framework that describes three of the four fundamental forces of nature, described in more detail in Chapter 2. Despite apparent completeness after the Higgs discovery, it is known that the theory does not describe gravity, the fourth of the known fundamental forces of nature. The theory also has other shortcomings, it cannot explain the presence of dark matter [13–23] or a number of other observed phenomena [24–28]. So far the model has stood up to all experimental tests [29, 30] concerning its own predictions but there are still parameters of the model that have not been measured. Given the theory’s understood shortcomings, it is hoped that continued scrutiny of the models predictions will yield unexpected results, perhaps hinting at a new way forwards in terms of a theory that describes everything or simply exposing further gaps in our knowledge of the universe. For this reason it is more important than ever to study in detail the most recently discovered piece of the model, the Higgs boson.

This work focuses on studying a specific production mechanism and decay mode of the Higgs boson, specifically a vector boson associated Higgs boson decaying to two bottom quarks, denoted  $VH(bb)$ . This decay mode is of importance as it is currently the only decay mode of the Higgs decaying to quarks that has been observed [31]. A summary of the full spectrum of production mechanisms and decay modes of the Higgs will be given in Chapter 2.

The study of this decay mode was carried out with the ATLAS detector, and made possible by the hard work of all members of the ATLAS collaboration. In Chapter 3 the detector is

described in full.

# Chapter 2

## Physics Theory

The following chapter outlines the physics theory that informs and guides the experimental process of searching for new particles or making measurements at a particle collider. Not only are the physics theories described here useful in that context but they also provide an almost complete picture of the universe at certain scales. This chapter was written with the aid of notes taken at the annual STFC High Energy Physics Summer School, and with the aid of several books [32, 33], in which a more detailed description of the theories can be found.

The Standard Model of particle physics is a theoretical framework that describes all elementary particles and three of the fundamental forces of nature. Notably the only force that is not described by the theory is gravity. Particles described by the model are listed in table 2.1 with a white gap separating the matter particles (fermions) from the force carrying particles (bosons). Fermions which make up solid matter obey Fermi-Dirac statistics [34, 35] whereas bosons obey Bose-Einstein statistics [36]. The Higgs boson is special in that as far as we know it does not carry a force in the conventional sense, instead it is responsible for giving particles mass via a mechanism described in the following. In the table of particles quarks (blue) and leptons (red) are ordered in columns by increasing mass, apart from the neutrinos whose absolute mass is not known, and in fact not predicted by the model.

As mentioned the model describes forces as being mediated by certain particles, the photon ( $\gamma$ ) mediates the electromagnetic force, particles experiencing electromagnetic repulsion or attraction are described as exchanging photons. The strength and direction of the force experienced is proportional to the electromagnetic charge of particles involved. The Standard Model

<i>u up quark d down quark</i>	<i>c charm quark s strange quark</i>	<i>t top quark b bottom quark</i>	<i>g gluon <math>\gamma</math> photon</i>	<i>H Higgs</i>
<i><math>e^-</math> electron <math>\nu_e</math> electron neutrino</i>	<i><math>\mu^-</math> muon <math>\nu_\mu</math> muon neutrino</i>	<i><math>\tau^-</math> tau <math>\nu_\tau</math> tau neutrino</i>	<i><math>Z^0</math> <math>Z</math> boson <math>W^\pm</math> <math>W</math> boson</i>	

Table 2.1: The particles of the standard model with fermions displayed on the left and bosons on the right. Quarks are in blue, leptons in red, vector bosons in yellow and scalar bosons in green.

is a theory of quantum fields in which the strength of interactions between fields, or particles which are described as excitations in the fields, is parametrised by something known as a coupling constant. It is natural to assume that the strength of the interaction between photons and charged particles is in some way related to the electromagnetic charge of the particles involved. Indeed this is the case consider the Coulomb force between two protons,

$$F = \frac{e^2}{4\pi\epsilon_0 r}, \quad (2.1)$$

where  $e$  is the elementary charge,  $\epsilon_0$  is the electric constant and  $r$  is the distance between the two protons in question and also the energy of a photon given by

$$E = \frac{hc}{\lambda}, \quad (2.2)$$

where  $h$  is Planck's constant,  $c$  is the speed of light and  $\lambda$  is the wavelength of the photon. The value of the ratio of these two quantities

$$\alpha = \frac{e^2 \lambda}{4\pi\epsilon_0 r h c}, \quad (2.3)$$

known as the fine structure constant, is the coupling constant that describes the strength of the interactions between the photon field and fields of particles with electromagnetic charge. So as is now clear this coupling constant does indeed depend on the electromagnetic charge of the objects involved and so it not really constant.

As well as the electromagnetic force the Standard Model describes the strong nuclear force and the weak nuclear force, shortened to just the strong and weak forces respectively. Like the electromagnetic force they too are mediated by the exchange of particles, namely the gluons ( $g$ ) carry the strong force and the  $W^\pm$  and  $Z^0$  bosons carry the weak force.

The charge associated with the strong force is known as colour which can take values that are mapped onto colours in the visible spectrum (red, green, blue) for ease of description. For each of these colours an anti-colour is also allowed (anti-red, anti-green, anti-blue). Unlike with the electromagnetic charge particles with colour charge are not found freely in nature. Instead we find particles known as hadrons which are bound states of quarks and anti-quarks (e.g. the proton). The phenomenon of coloured particles being bound in such a manner is known as colour confinement, and the bound states are described by the quantum numbers isospin ( $I$ ) and hypercharge ( $Y_c$ ). It is assumed but not proven that all free particles in nature are colour singlets e.g. for a hadron the state could be written as

$$\frac{(r\bar{r} + b\bar{b} + g\bar{g})}{\sqrt{3}}, \quad (2.4)$$

where  $r$ ,  $b$  and  $g$  represent red, blue and green charges respectively. Gluons carry colour and anti-colour indicating that there should be nine possible quantum mechanical states for the gluon given the available number of colour anti-colour combinations, however when one considers that the strong force is exclusively short range, and therefore that there should be no free gluons (disallowing colour singlet gluons) the number of possible states is reduced to eight. The state of a particle, as far as its description with respect to the strong force is concerned, is given by a vector which lives in a vector space in which elements of the Lie group  $SU(3)_C$  act as unitary operators, where the  $C$  denotes that the group is associated with the colour charge. The  $SU(3)$  group is the group of  $3 \times 3$  unitary matrices whose determinant is one. These correspond to the eight generators of  $SU(3)$  where in general for a group  $SU(N)$  the number of generators is given by  $N^2 - 1$ .

Describing the weak force requires introducing further quantum numbers weak isospin  $T$  and weak hypercharge  $Y_W$ . The state of a particle with regards to the weak force is given by a vector which lives in a vector space in which elements of  $SU(2)_L \times U(1)_{Y_W}$  act as unitary

operators where the  $L$  denotes that only particles in left-handed chiral states interact with the weak force<sup>1</sup>. Left-handed fermions are represented as doublets in the theory with weak isospin  $T = 1/2$  whilst right-handed fermions are singlets with weak isospin  $T = 0$ .

Along the way we have described particle states with respect to particular forces as being vectors living in some vector space where the action of the element of a group has been as a unitary operator. If we are to describe a particle state taking into account the full model the group whose elements should act as unitary operators on the particle state (the gauge group) is  $SU(3)_C \times SU(2)_L \times U(1)_{Y_W}$ . For each of the groups in the direct product we have established a (gauge) symmetry and therefore due to Noether's theorem there should be an associated conserved quantity. The conserved quantities in this case are the electric charge, the weak hypercharge and isospin and the colour charge.

## 2.1 Historical Aside

This section provides some historical context surrounding the Dirac equation which will later be used as the starting point in the discussion of quantum electrodynamics, which is the sector of the Standard Model that describes electromagnetic interactions.

In 1905 Albert Einstein first proposed the idea of special relativity [37]. The aim of the idea was to unify the then inconsistent theories of Maxwell's electromagnetism and Newtonian mechanics. The result of Einstein's work was a theory of motion which agreed with the predictions of Newtonian mechanics at velocities much smaller than the speed of light but whose predictions were accurate also at much higher velocities (for which Newtonian predictions fail). Arguably the most far reaching consequence of special relativity is that it demands that any equation of motion must be invariant under Lorentz transformations, at least in terms of the formulation of new theories is concerned. Many physical phenomena predicted by special relativity could be considered of higher consequence in general, for example the phenomena of length contraction, time dilation, energy-mass equivalence and the universal speed limit (equal to the speed of light in vacuum), all of which are extensively scrutinised experimentally [38–44]. It is the Lorentz transformation however that should be kept in mind for the following discussion, the

---

<sup>1</sup>More specifically only left-handed chiral particles participate in weak charged current interactions.

transformation may be written as

$$\begin{aligned} t' &= \gamma(t - vx/c^2) \\ x' &= \gamma(x - vt) \\ \text{with } \gamma &= \frac{1}{\sqrt{1 - v^2/c^2}}, \end{aligned} \tag{2.5}$$

in a single dimension of space  $x$  and one of time  $t$  where  $v$  represents the velocity of the system described by the primed coordinates relative to the unprimed coordinates and  $c$  is the speed of light in vacuum.

Twenty years after Einstein introduced the ideas of special relativity Erwin Schrödinger postulated new ideas regarding the motion of quantum mechanical systems [45]. Though he knew his new equation was not invariant under Lorentz transformations and therefore incomplete Schrödinger's formulation of quantum mechanics changed the way physicists thought about the universe for ever. His famous equation

$$i\hbar \frac{\partial}{\partial t} \Psi(\vec{x}, t) = \left( \frac{-\hbar^2}{2m} \nabla^2 + V(\vec{x}, t) \right) \Psi(\vec{x}, t), \tag{2.6}$$

describes the states of particles as wave-functions  $\Psi$  which can only be interpreted in a probabilistic manner and contains Planck's constant the quantum of action. This work had many consequences including the quantisation of the values of measured observables (meaning they can only take discrete values) and the descriptions of particles as waves.

It was the aim of Paul Dirac to make the Schrödinger equation Lorentz invariant and thus provide a more complete description of quantum systems. Along the way he came to the realisation that in order for his equation to satisfy his needs the wave-function had to be replaced with a four component spinor ( $\psi$ ) and the introduction of matrices known now as the Dirac matrices (labeled  $\gamma^\mu$  with  $\mu = 0, 1, 2, 4$ ) was required. Though not the form he originally wrote down Dirac's Lagrangian density takes the form

$$\mathcal{L}_{Dirac} = \bar{\psi}(i\gamma^\mu \partial_\mu - m)\psi, \tag{2.7}$$

where the repeated up and down indices are implicitly summed over ( $\partial_\mu$  represents the partial derivative taken with respect to a spatial coordinate  $\mu = 1, 2, 3$  or time  $\mu = 0$ ).

## 2.2 Quantum Electrodynamics

In order to take Dirac's Lagrangian (eq. 2.7) and turn it into something that appropriately describes quantum electrodynamics (QED) we should consider a  $U(1)$  gauge transformation of the Dirac spinor and its adjoint

$$\begin{aligned}\psi \rightarrow \psi' &= e^{i\alpha(x)}\psi, \\ \bar{\psi} \rightarrow \bar{\psi}' &= e^{-i\alpha(x)}\bar{\psi},\end{aligned}\tag{2.8}$$

with  $\bar{\psi} \equiv \psi^\dagger \gamma^0$  and where  $\alpha(x)$  is a local phase. Under this transformation the Lagrangian transforms as

$$\mathcal{L}_{Dirac} \rightarrow \mathcal{L}'_{Dirac} = \bar{\psi}(i\gamma^\mu \partial_\mu - m)\psi - \bar{\psi}\gamma^\mu \alpha(x)\psi\tag{2.9}$$

which is not equivalent to the original due to the factor resulting from the derivative of the transformed spinor. Instead let us change the derivative to the gauge covariant derivative

$$D_\mu = \partial_\mu + ieA_\mu\tag{2.10}$$

where we interpret  $A_\mu$  as the photon field with coupling constant  $e$  parametrising the interaction strength. The field is also referred to as the electromagnetic gauge field since it arrives during the process of making the Lagrangian invariant under the  $U(1)$  group, the gauge group of electromagnetism. Note that here what we have labeled  $e$  is nothing more than the fine structure constant previously denoted  $\alpha$  in eq. 2.3. The transformation of the new field under the action of the gauge is defined as

$$A_\mu \rightarrow A'_\mu \equiv A_\mu - \frac{1}{e}\partial_\mu \alpha(x).\tag{2.11}$$

This means that the action of the gauge covariant derivative on the spinor transforms as

$$D_\mu \psi \rightarrow D'_\mu \psi' = e^{i\alpha(x)} D_\mu \psi\tag{2.12}$$

which means that the new Lagrangian

$$\mathcal{L} = \bar{\psi}(i\gamma^\mu D_\mu - m)\psi \quad (2.13)$$

is invariant under the action of the gauge as desired. What remains in order to write a description of QED is to write down a kinetic term for the photon field. An appropriately gauge and Lorentz invariant term is

$$-\frac{1}{4}F_{\mu\nu}F^{\mu\nu} \quad (2.14)$$

where the electromagnetic tensor is defined as

$$F_{\mu\nu} \equiv \partial_\mu A_\nu - \partial_\nu A_\mu. \quad (2.15)$$

Putting everything together we can define the Lagrangian for QED as

$$\mathcal{L}_{QED} = \bar{\psi}(i\gamma^\mu D_\mu - m)\psi - \frac{1}{4}F_{\mu\nu}F^{\mu\nu} \quad (2.16)$$

## 2.3 Quantum Chromodynamics

Quantum Chromodynamics (QCD) is the theory of the strong force. It's mathematical formulation is similar to that of QED. Except the gauge group for QCD is  $SU(3)_C$  where the  $C$  denotes that the force is associated with colour charge. As previously discussed the eight generators of the group are associated with the eight gluons of the Standard Model. The generators are present in the form of the transformation of a fermion field under an element of  $SU(3)$

$$\psi \rightarrow \psi' = \exp\left(i\alpha_a(x) \cdot \frac{\lambda_a}{2}\right)\psi, \quad (2.17)$$

where the  $\lambda_a$  are the Gell-Mann matrices, generators of  $SU(3)$ . A key difference between the strong force and the other forces described by the Standard Model is that it increases in strength with range. This property leads to a phenomena known as quark confinement which has been discussed previously. Quark confinement is the reason for many of the complications that arise

when trying to detect certain particles in a particle detector such as ATLAS. Specifically quarks that are produced in collisions undergo a process called hadronisation whereby they transition from their coloured states to colour singlets. Excess energy present in this process results in the creation of lots of different states some which decay leptonically and the overall process produces a large conical shower of particles known as a jet.

## 2.4 Electroweak theory

The Glashow-Salam-Weinberg model of electroweak interactions [46–48] describes the weak force and electromagnetism as a quantum field theory which is gauge invariant under transformations which are elements of  $SU(2)_L \times U(1)_{Y_W}$ . As previously mentioned the  $L$  and  $Y_W$  subscripts denote that the gauge groups in the direct product that are associated with left-handed chiral particles and weak hypercharge respectively. The association with weak hypercharge distinguishes this  $U(1)$  group with the  $U(1)$  group from QED. The transformation of the fermion fields under  $SU(2)$  is given by

$$\psi \rightarrow \psi' = \exp\left(i\vec{\alpha}(x) \cdot \frac{\vec{\sigma}}{2}\right)\psi, \quad (2.18)$$

where  $\vec{\sigma}$  is a vector of the Pauli matrices  $\sigma_i$  with  $i = 1, 2, 3$ , a familiar representation of  $SU(2)$  generators. Constructing a gauge covariant derivative for the full transformation under  $SU(2) \times U(1)$  requires the addition of new fields analogous to the photon field from QED, the new derivative takes the form

$$D_\mu = \partial_\mu - i\frac{g_1}{2}Y_W B_\mu - i\frac{g_2}{2}\sigma_i W_\mu^i, \quad (2.19)$$

where coupling constants  $g_1$  and  $g_2$  parametrise the strength of interactions with each field. The index  $i$  runs over the three Pauli matrices and three new fields  $W_\mu^i$  with  $i = 1, 2, 3$  which are associated with the  $SU(2)$  gauge. The  $B_\mu$  field is associated with the  $U(1)_{Y_W}$  gauge and is obtained in the same way as the photon field in QED but is given a new symbol as it is *not* the photon field.

In fact none of the fields added here are the physical fields that we have access to in nature

associated with the electromagnetic force or the weak currents. In order to obtain the physical fields for the weak charged current one can simply take the linear superposition

$$W_\mu^\pm = \frac{1}{\sqrt{2}}(W_\mu^1 \mp iW_\mu^2). \quad (2.20)$$

In order to recover the photon field and reveal the field for the weak neutral current the idea of weak mixing must be introduced. Weak mixing was introduced to theory after the discovery of parity violation [49]. Parity is equivalent to chirality for massless particles, however for particles with mass a Lorentz boost can always appear to flip the chirality of the particles state whereas parity is a fundamental property of a particle. A fermion field with left or right handed chirality can be obtained by multiplication with one of two corresponding projection operators defined as

$$\begin{aligned} P_L &= (1 - \gamma^5)^2/2, \\ P_R &= (1 + \gamma^5)^2/2, \end{aligned} \quad (2.21)$$

with  $\gamma^5 = i\gamma^0\gamma^1\gamma^2\gamma^3$ , where  $\gamma^\mu$  are the Dirac matrices, like so

$$\begin{aligned} \psi_L &= P_L\psi, \\ \psi_R &= P_R\psi. \end{aligned} \quad (2.22)$$

It is known that the weak neutral current and indeed the electromagnetic force both interact with particles of left and right handed chirality. Spontaneous symmetry breaking, theorised to have occurred due to an electroweak phase transition in the early universe, has the effect of rotating the plane defined by the  $B_\mu$  and  $W_\mu^3$  fields into the physical fields we see in nature today. The mixing of the fields due to this rotation takes the form

$$\begin{pmatrix} A_\mu \\ Z_\mu \end{pmatrix} = \begin{pmatrix} \cos \theta_W & \sin \theta_W \\ -\sin \theta_W & \cos \theta_W \end{pmatrix} \begin{pmatrix} B_\mu \\ W_\mu^3 \end{pmatrix}, \quad (2.23)$$

where  $\theta_W$  the Weinberg angle parametrises the amount of mixing. This picture shows that unification of QED and a description of the weak force has been achieved. Although it at first

seems like the  $U(1)_{EM}$  gauge group is not present in  $SU(2)_L \times U(1)_{Y_W}$  gauge group of electroweak theory it has been shown that the QED gauge symmetry is recovered by spontaneous symmetry breaking. Also the  $Y_W$  subscript in the gauge group represents weak hypercharge which is related to electric charge  $Q$  by the following relationship

$$Y_W = 2(Q - T^3), \quad (2.24)$$

where  $T^3$  is the third component of isospin, the component that is conserved.

The particles associated with the weak neutral and charged currents are observed to have masses in nature [50–53] therefore one would naively like to write mass terms of the form

$$\mathcal{L}_{mass} \propto M_B^2 B^\mu B_\mu \quad (2.25)$$

$$+ M_W^2 W_a^\mu W_\mu^a. \quad (2.26)$$

The above mass terms are however not gauge invariant therefore another solution is required, one which will be discussed in the next section.

## 2.5 The Brout-Englert-Higgs Mechanism

The Brout-Englert-Higgs mechanism was made complete almost simultaneously by R. Brout and F. Englert [54], P. Higgs [55] and, G. Guralnik, C. R. Hagen and T. Kibble [56]. The underlying mechanism was proposed prior to this work by P. Anderson [57], though this initial theory was not relativistic invariant. It was initially proposed as a means to give the vector bosons mass terms that were gauge invariant. The theory predicts a complex scalar field (the Higgs field) that undergoes spontaneous symmetry breaking. Interactions with this field are predicted to be mediated by a massive spin-1 scalar particle that is now known to be the Higgs boson. This particle also gives mass to the fermions via a different mechanism. Spontaneous symmetry breaking is a process by which a symmetry breaks once conditions meet some threshold. An example of this is a hot sphere of ferromagnetic material whose spins are isotropically oriented. As the sphere cools the ferromagnetic property of the material will

align the spins. In the hot scenario the sphere had symmetry in all spatial directions, by this it is meant that the changes to the sphere's orientation were indistinguishable. Once the spins have aligned however this is no longer the case, the fact that the spins point in a specific direction means that direction is special and so some of the symmetry was spontaneously broken. It can be noted though that a preserved symmetry still exists as rotations about the axis defined by the direction of the spins would leave the sphere invariant. In the Standard Model the symmetry that breaks is that of the complex scalar Higgs field. Consider a Lagrangian involving the field  $\phi$  of the form

$$\mathcal{L} = T - V(\phi) = \partial_\mu \phi^\dagger \partial^\mu \phi - \mu^2 \phi^\dagger \phi + \lambda (\phi^\dagger \phi)^2, \quad (2.27)$$

$$\text{with } \phi = \frac{1}{\sqrt{2}}(\phi_1 + i\phi_2). \quad (2.28)$$

Invariance under global phase transformations of the form  $\phi \rightarrow e^{i\theta}\phi$  depends on the parameters of the potential  $\mu$  and  $\lambda$ . Figure 2.1 shows two sketches of the potential for the scenarios where  $\mu^2 > 0, \lambda < 0$  (left) and  $\mu^2 < 0, \lambda < 0$  (right). To suggest that in our universe this symmetry

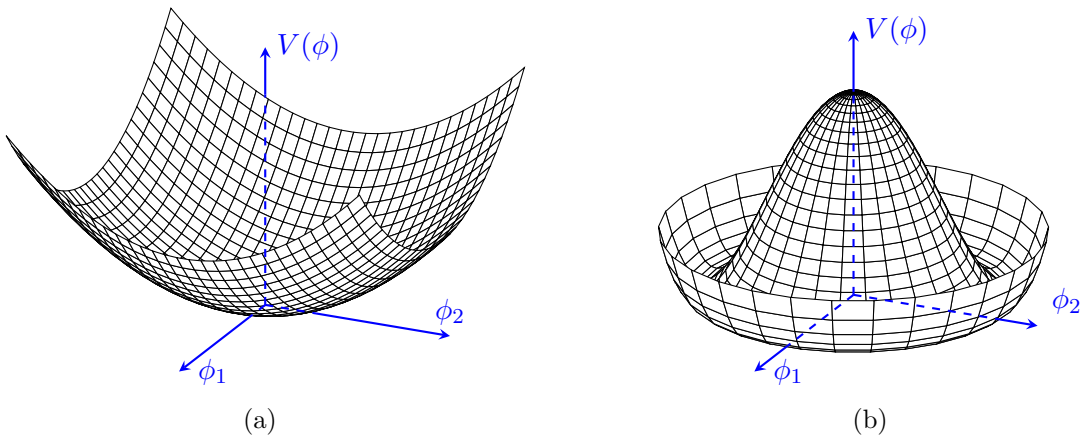


Figure 2.1: The Higgs potential in its fully and broken symmetric forms.

is spontaneously broken is to suggest that the values of these parameters evolved over time from the full to the broken state. This ends up leading to masses for the vector bosons that are dependent on  $\mu^2$ .

## 2.6 Higgs bosons at the LHC

Higgs bosons are produced at the LHC in a number of different ways, the four most common of which are shown in figure 2.2. The prevalence of these processes with respect to the centre

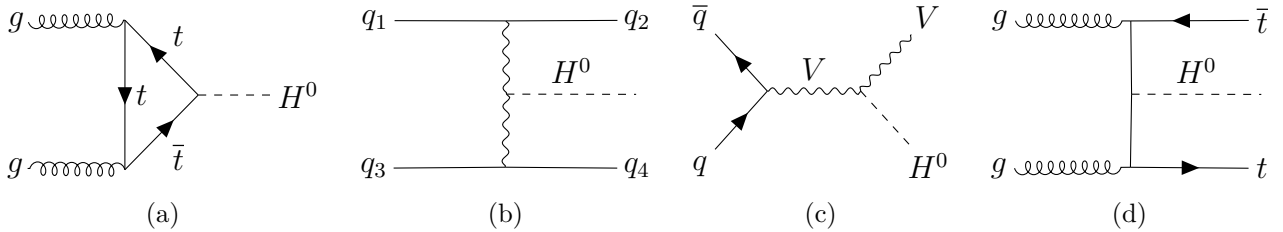


Figure 2.2: The four most common Higgs boson production methods from proton-proton collisions at the LHC.

of mass energy of the proton-proton collision is shown in figure 2.3 (a). It can be seen the gluon-gluon fusion (fig 2.2 a) is by far the dominate contributor occurring over an order of magnitude more than the next highest process which is quark associated production (fig 2.2 b). The next highest production channel with respect to cross section is vector boson associated (fig 2.2 c) which will be the focus of the rest of this report. Finally top quark associated production (fig 2.2 d) has the smallest cross section of these processes. The Higgs boson is predicted by the Standard Model to decay in a number of different ways depending on its mass, a free parameter of the model. In figure 2.3 (b) the branching ratios of the Higgs can be seen, plotted with respect to Higgs mass. The decay that will be focused on for the rest of this report is  $H \rightarrow b\bar{b}$ . Given that the focus here is on vector boson associated production of a Higgs boson it is also important to consider the decay of the vector boson. Three possible scenarios are represented in figure 2.4, namely the situations where the vector boson decays to 1, 2 or 3 charged leptons and the appropriate number of neutrinos. It is in fact these leptonic decay modes that motivate the reason for studying this production mechanism as opposed to one of the more common ones. The issue with looking at the other production modes is that very large QCD generated backgrounds are present due to initial state radiation. Whilst these backgrounds are also present when looking at the vector associated channel they can be partially suppressed by triggering on a lepton.

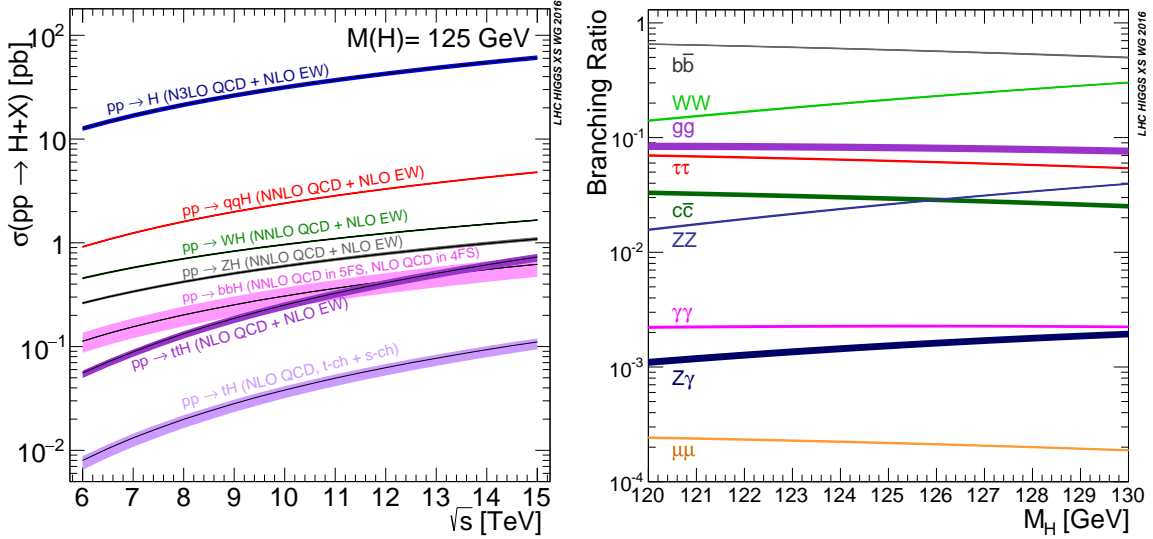


Figure 2.3: Higgs production cross-sections (left), and branching ratios (right) for a range of centre of meass energies and Higgs boson masses respectively [1].

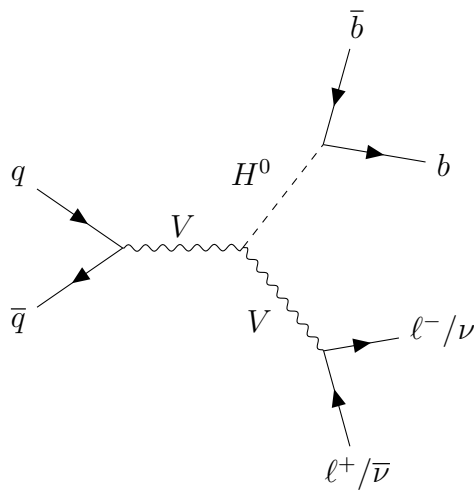


Figure 2.4: A diagram showing a Higgs boson (decaying to a pair of b quarks) produced in association with a vector boson (decaying to 0, 1, or 2 charged leptons denoted  $\ell^{+/-}$ ).

# Chapter 3

## The ATLAS Detector at the Large Hadron Collider

### 3.1 The Large Hadron Collider

The Large Hadron Collider (LHC) [58] is a large circular machine located 100 m underground straddling the Swiss-French border at the European Organisation for Nuclear Research (CERN). The machine is primarily a proton collider<sup>1</sup> and is circular in design so that protons may be accelerated over many revolutions to high energies before being allowed to collide. The diameter of the LHC is 27 km, the tunnel in which the machine resides was originally excavated for the LEP [59] experiment and at the time was the largest civil engineering project in Europe. There are many experiments at CERN all with the goal of improving our understanding of a particular area of physics some of which are marked in figure 3.1. In particular there are seven experiments that record data from the collisions at the LHC: ATLAS [60], CMS [61], LHCb [62], ALICE [63], MoEDAL [64], TOTEM [65] and LHCf [66].

The LHC receives protons that have already been accelerated somewhat by the Super Proton Synchrotron (SPS), another of the accelerators at the CERN accelerator complex shown in figure 3.1. The circular design of both the LHC and SPS allows protons to be accelerated many times around their respective rings until their velocity is fast enough for a high energy collision. The highest energy collisions achieved at the time of writing take place at a centre of

---

<sup>1</sup>The LHC also collides other charged particles such as ions of lead or xenon.

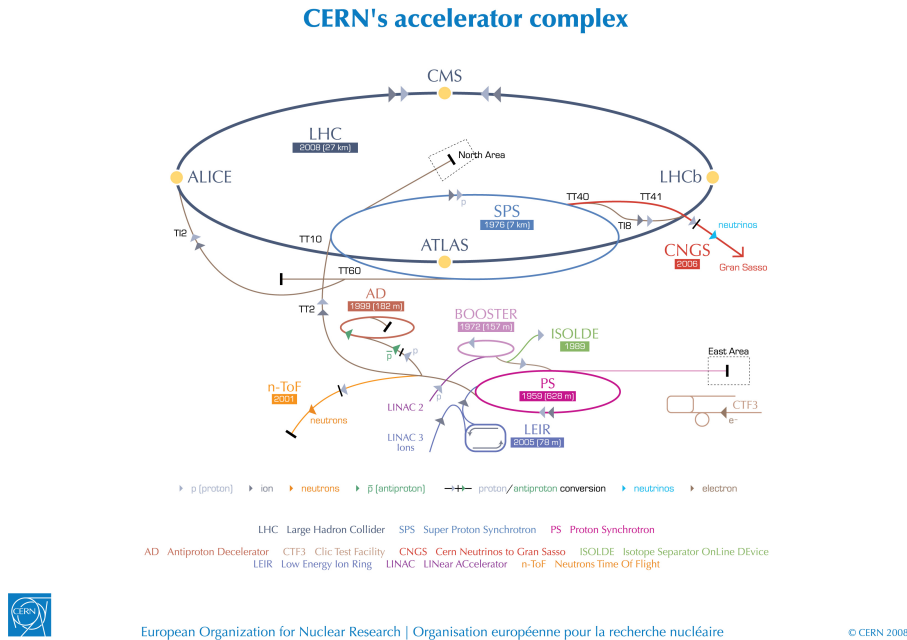


Figure 3.1: The CERN accelerator complex [2].

mass energy of  $\sqrt{s} = 13$  TeV, although the design energy of the LHC is  $\sqrt{s} = 14$  TeV. Despite having not yet reached its design energy the LHC collides particles with the highest energy of any particle collider in history and is currently alone at the energy frontier of modern physics. At the time of writing the LHC is in its second long shutdown during which maintenance and upgrades to the LHC and the particle detectors located around its ring take place. The LHC has completed two main runs of collisions Run 1 took place between 2009 and 2013, followed by a long shutdown period and then Run 2 between 2015 and 2018. Many analyses from Run 1 have been published including most notably the discovery of the Higgs boson [11, 12]. Some Run 2 analyses have also published results notably LHCb's discovery of charge parity violation in charm decays [67]. Despite these impactful results there are many more results expected from the LHC experiments as data continues to be analysed.

The statistical nature of particle physics analyses means that larger datasets (more recorded collisions) increase the sensitivity of searches and measurements. Constraints on the number of years the LHC is able to run mean that the best way to record more collisions is to collide more particles per second. A quantity known as the luminosity is often used to describe how much data is available for an analysis, it is written as

$$L = \frac{1}{\sigma} \frac{dN}{dt}, \quad (3.1)$$

where  $\sigma$  is the interaction cross-section, a volume within which particles must pass by one another in order to interact, and  $N$  is the number of events recorded in a period of time  $t$ . For luminosity at the LHC  $N$  can be expressed as

$$N = n_{bp}n_1n_2\nu_r, \quad (3.2)$$

where  $n_{bp}$  is the number of colliding bunch pairs,  $n_1$  and  $n_2$  are the number of protons in each beam and  $\nu_r$  is the frequency with which the beams rotate around the LHC's circumference. It is clear that to increase luminosity any one of these parameters can be increased. The LHC has already exceeded its design luminosity providing physicists with more data to analyse than expected and plans are well underway for the upgrade to a High-Luminosity LHC (HL-LHC) [68].

## 3.2 The ATLAS Detector

The ATLAS detector [69] resides at a location on the LHC ring called Point 1, its full name is A Toroidal LHC ApparatuS. A diagram of the detector is shown in figure 3.2. ATLAS is considered to be a general purpose particle detector and has a wide physics program including: Higgs boson physics, top quark physics, searches for Supersymmetry and exotic states, probes of CP violation in b-quarks and light states and heavy ion physics. The work in this report is concerned with the measurement of products from proton-proton collisions. The detector itself is very large in size, spanning a width of 25 m and a length of 44 m and weighs 7000 tonnes which is comparable to the weight of the wrought iron content of the Eiffel tower [70].

Due to the composite nature of the proton, the decay products of collisions are extremely numerous. Additionally when two bunches of protons cross there is the chance that more than one hard scattering event occurs and softer glancing collisions are also a possibility. The number of hard scattering events in a given bunch crossing is known as the pile-up of the collision and is often denoted with the symbol  $\mu$ . As can be seen by inspecting equation 3.2 increasing the luminosity will often cause a higher pile-up environment in the detector. High pile-up, along with the numerous decay products of each collision necessitate the use of specialised sub-

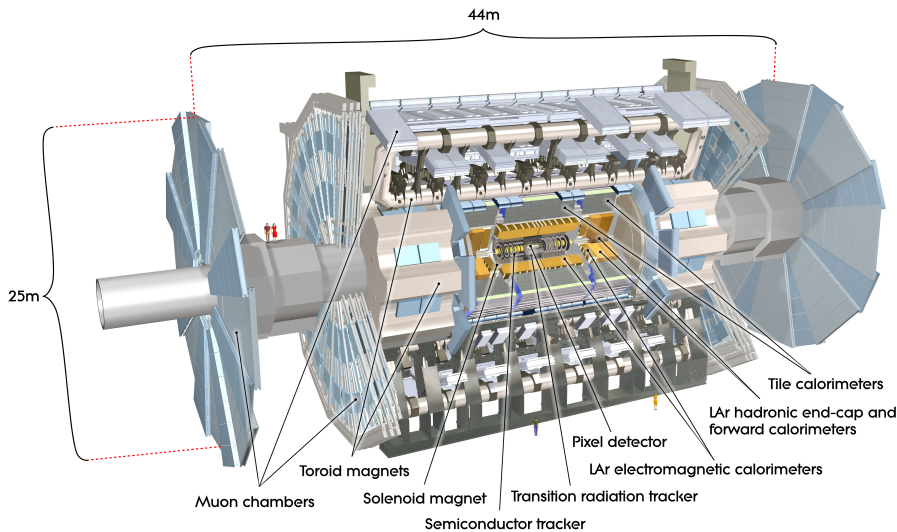


Figure 3.2: Computer generated image of the whole ATLAS detector with the major sub detectors labeled [3].

detectors in order to accurately measure the output of collisions. For certain types of decay product there are different dedicated sub-systems in ATLAS with the purpose of measuring properties of particles of that type. At this stage it is sufficient to say that the treatment of electrically charged particles must be different to those that are electrically neutral but this concept will be expanded upon in more detail in the further sections. It is interesting to note that despite the many charges that are associated with the forces of nature discussed in chapter 2 the only one that we can directly measure is electric charge<sup>2</sup>.

The ATLAS sub-systems are located in either the barrel of the detector or one of the end-caps. These two areas have a different geometry and so the design of a sub-system in the barrel will differ from the same sub-system in the end-cap. What follows is a description of the ATLAS sub-systems and their individual components, for each component more detail will be given about which properties of which types of particles it is used to measure. These details are based on the ATLAS technical design report volumes [71, 72] unless another citation is present. Before detailing individual components it is important to detail certain properties of the detector relevant to all sub-systems. The coordinate system used to describe the ATLAS detector is known as right-handed. Three orthogonal axes ( $x, y, z$ ) are used to describe the 3D

---

<sup>2</sup>This is true for current human technology, it is not known if future or alien technology can access other charges.

space of the detector. The x-axis points towards the centre of the LHC ring, the y-axis points upwards and the z-axis points along the LHC beam pipe y-axis. The three axes meet at the interaction point which is the nominal position where bunches cross, located in the centre of the detector. Cylindrical coordinates  $(r, \phi)$  are also often used to describe the physical features of the detector and phenomena caused by interactions in the detector that shall be referred to as analysis objects. Their definitions are that  $\phi$  is the azimuthal angle in the x-y plane (transverse) around the beam pipe and  $r$  is the distance from the interaction point. A final quantity used due to its compatibility with description relativistic objects in the detector is pseudo-rapidity  $\eta = -\ln(\tan(\theta/2))$  where  $\theta$  is the zenith angle measured from the z-axis.

The grouping of particles into electrically charged or neutral is largely due to the fact charged particles experience the Lorentz force

$$\vec{F} = q(\vec{E} + \vec{v} \times \vec{B}), \quad (3.3)$$

whereas neutral particles have  $q = 0$ , and so they do not. The magnetic field  $\vec{B}$  has the effect of changing the direction of the particles trajectory only. This is due to the fact that any force  $\vec{F}$  resulting from the cross product of two vectors, in this case the field vector and the velocity  $\vec{v}$ , must act in a perpendicular to the two crossed vectors and thus perpendicular to the direction of the motion (the direction of velocity). Similarly the electric field term  $\vec{E}$  has the effect that the particle is accelerated in the direction (or opposite in the case of a negative particle) of the field lines. The consequence of this is that in a known magnetic field the velocity of a particle can be calculated by measuring the radius of curvature of its trajectory. It also means that magnetic fields can be used to alter a particles path through a detection medium so that it passes through a greater amount of material than in the situation where its path was straight. In order to exploit these properties of charged particles a large portion of the ATLAS detector is immersed in magnetic fields created by the magnet systems. There are four magnet systems in ATLAS the solenoid, the barrel toroid, and two end-cap toroids. The solenoid surrounds the inner detector whilst the toroid systems surround the muon chambers. Figure 3.3 shows a heat map of the magnetic field strengths within ATLAS, the image is from an article detailing the superconducting magnet system [4]. The magnet systems store a total energy of 1.6 GJ and

produce fields of a combined volume of approximately  $12 \times 10^4$  m<sup>3</sup>.

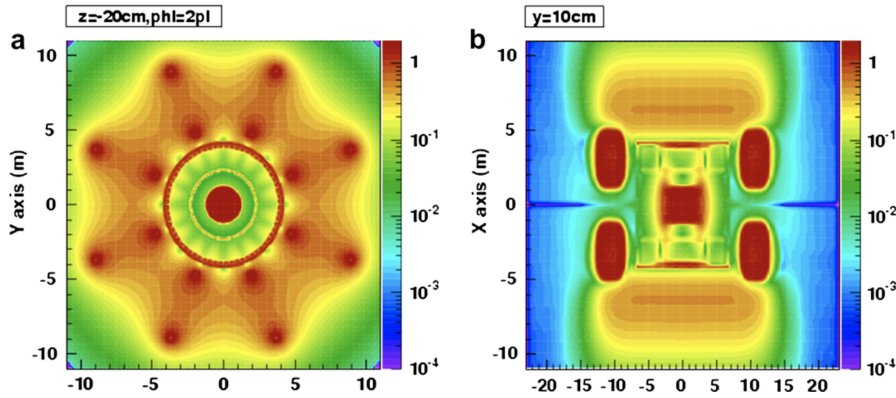


Figure 3.3: ATLAS magnetic field profile, showing a transverse cross-section in the centre of the detector (a), and a longitudinal section (b) [4].

## Inner Detector

The Inner Detector (ID) is comprised of pixel detectors, the semiconductor tracker (SCT) and a transition radiation tracker (TRT) as seen in figure 3.4. It covers a volume corresponding with the total  $\phi$  angle. In relation to  $\eta$  the pixel detectors and SCT cover the range  $|\eta| < 2.5$  and the TRT covers  $|\eta| < 2.0$ . Being the innermost sub-detector of ATLAS the primary goals of the ID are to reconstruct the locations of the origin of interactions (known as the interaction vertex), and to track the propagation of charged particles through the detector. This is achieved by measuring a sequence of hits for each charged particle that propagates through its material, upon which reconstruction algorithms can be applied known as track finding algorithms. From this sequence of hits interaction vertices can also be reconstructed, the vertex which comes from the highest energy collision in a given event is known as the primary vertex. By using the combined information the vertices and tracks decay products in more outer regions of the detector can be matched with their vertices. Each reconstructed track will have a momentum assigned to it, which is calculated using equation 3.3. The magnetic field that the ID is immersed in is produced by the solenoid magnet system. The system is made of a single layer coil with an inner diameter of 2.46 m and produces 2 T field in the axial direction with respect to the beam-pipe.

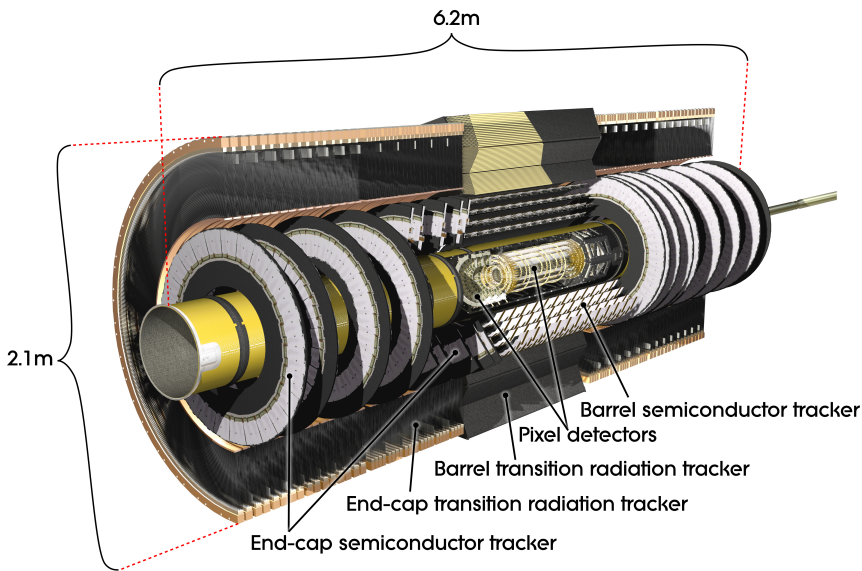


Figure 3.4: Computer generated image of the ATLAS inner detector [5].

## Pixel Detectors

There are four layers of pixel detectors that are the closest components of the ID to the beam-pipe. The design originally had three layers, each  $250\ \mu\text{m}$  thick with  $50\ \mu\text{m}$  by  $250\ \mu\text{m}$  pixels, of oxygen doped n-type silicon crystals. During the first long shutdown a fourth layer, closest to the beam-pipe (which was also replaced for a smaller radius version) was added. This layer is known as the insertable B-layer (IBL) [73], the motivation for its addition was to maintain the existing performance of the ID despite irreversible damage to the original three pixel layers due to heavy radiation exposure. As well as the inclusion of the IBL performance degradation will be mitigated by increasing the bias voltage across the pixels from 100 V (their starting voltage) to up to 600 V. There are no pixel detectors in the end-caps.

## Semiconductor Tracker

Next closest to the beam-pipe are the semiconductor trackers. Similarly to the pixel detectors the semiconductor trackers are also made of silicon. In contrast the n-type silicon of the pixels, the semiconductor trackers use p-in-n type technology. The semiconductor modules are comprised of two back to back silicon wafers that are offset by a small angle in order to improve coverage. Each wafer has a series of strips of p-in-type material covered in a metalised layer, the strips are separated by a distance of  $80\ \mu\text{m}$ . The strips have a bias voltage applied and on

the wafers the necessary electronics are mounted for readout as seen in figure 3.5. In order to



Figure 3.5: An image of an SCT long strip module mounted in a rig for testing at Queen Mary University of London.

calibrate the response of the strips a  $100\text{ M}\Omega$  poly-silicon resistor is located at the end of each strip. Figure 3.6 shows an image of the snake-like structure of a poly-silicon resistor from the end of an SCT module. The modules come in two different designs, short strips and long strips

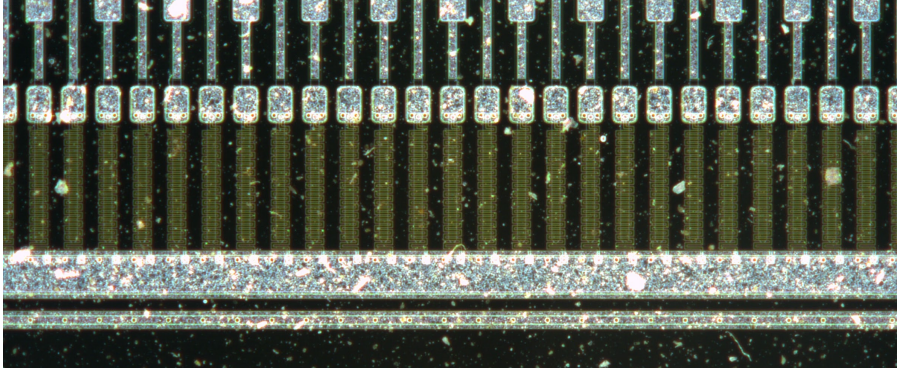


Figure 3.6: A close up image of the end of an SCT sensor in which the snake-like poly-silicon resistors are visible as a yellowish coloured structure at the end of each strip. This image was taken with a high resolution automatic area scanner commissioned by the author [6] in order to take full scans of strip sensors during the production of the ATLAS Inner Detector upgrade known as the Inner Tracker (ITk) [7, 8].

with the short strips forming the layer closest to the pixel detectors and the long strips on the outside.

The original operating bias voltage was 150 V but again due to radiation exposure this will raise to up to 350 V over time as necessary. There are four layers of semiconductor trackers

in the barrel arranged so that sensors have a tilt with respect to a perfect coaxial cylinders of approximately  $11^\circ$ . This tilt increases the amount of material that particles will travel through and is optimized to the geometry of the detector. Similarly the end-cap modules are arranged in petal like structures, with a number of different geometric designed based on the position within the end-cap.

### Transition Radiation Tracker

The final layer of the ID is the TRT, the primary role of the TRT is to aid electron identification by measurement of transition radiation. The TRT is mostly made up of polyimide drift tubes with a diameter of 4 mm. The drift tubes are filled with a gas mixture whose majority constituent is xenon. These tubes operate with a voltage of -1530 V and are contained within a carbon fibre support structure. The geometric layout of the tubes is optimized for both the barrel and end-caps.

### Calorimeters

The purpose of the calorimeters is two-fold, firstly the measure the energy of particles that pass all the way through the ID, and secondly to act as a barrier to stop charged particles passing through to the muon spectrometers (apart from muons). There are two calorimeter systems in ATLAS the electromagnetic calorimeter (ECAL) and the hadronic calorimeter (HCAL), they will be explained in the following sections. The calorimeters are not immersed in a significant magnetic field compared to the rest of the ATLAS as seen in the heat map of figure 3.3. This is because measuring the energy of particles and acting as a barrier to them does not require curved trajectories. The geometric layout of the calorimeter systems, as well as the location of specific components can be seen in figure 3.7, in which the ID can also be seen (greyed out). Information from the two calorimeters is used in conjunction for any particles whose decay products propagate through both volumes. Both calorimeters are split up into cells of material that are used to determine the position of decay products in the detector.

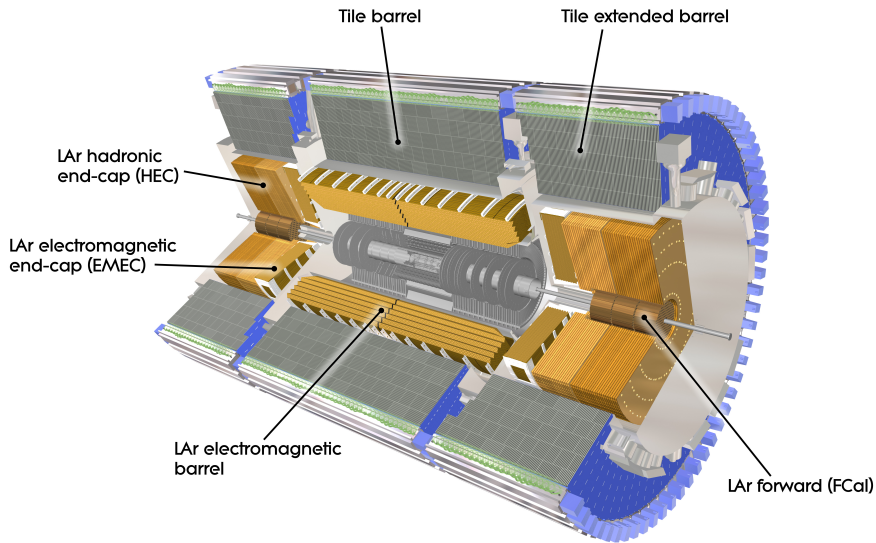


Figure 3.7: Computer Generated image of the ATLAS calorimeter [9].

### Electromagnetic Calorimeter

The ECAL is primarily concerned with measuring the energy and stopping the trajectory of electrons and photons. It has liquid argon (LAr) as its active material. Particles initiate an electromagnetic shower of decay products in the active material which ionizes it. An applied electric field causes these ions to drift in such a way that the current induced proportional to the energy deposited by the incident particle.

### Hadronic Calorimeter

The HCAL also has a LAr component which works in a similar way to that of the ECAL but with different optimizations for the HCAL's specialised design. The HCAL is specifically tasked with measuring the energy and stopping the trajectory of hadrons. The HCAL also contains a tile calorimeter which uses scintillation light produced in the tiles as a means to measure the deposited energy of hadrons.

### Muon Spectrometers

Surrounding the calorimeters are the muon spectrometers, which form the most outer layer of the detector. Though muons are charged leptons just like electrons, their specific properties

mean that dedicated muon spectrometers are required to detect them. Muons deposit far less energy per distance traveled than other particles meaning that they punch through most materials with ease. As can be seen in figure 3.8 the components of the muon spectrometers are the thin-gap chambers, cathode strip chambers, resistive plate chambers and monitor drift tubes. The barrel and end-cap toroid magnets immerse the muon spectrometers in a magnetic field which at its peak (visible in figure 3.3) has a strength of 4 T. Despite a stronger peaking magnetic field than in the solenoid observed muon tracks are often far less curved than that of their lighter cousins the electrons. This is due to the increased mass of the muon. Muons do leave tracks in the ID and also deposit small amount of energy in the calorimeters. Tracks in the muon spectrometers are matched up to tracks in the ID with the aid of the location of energy deposits in the calorimeters if possible. The full tracking information for muons can be used in algorithms such as overlap removal, which is used to remove muons from jets that they have been erroneously associated with by matching the muon with its ID track.

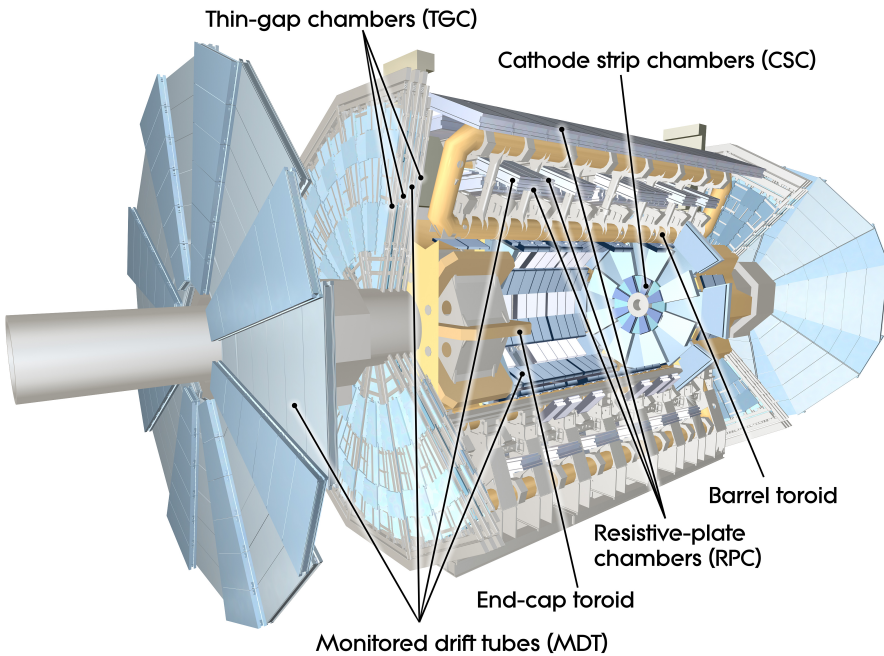


Figure 3.8: Computer generated image of the ATLAS Muons subsystem [10].

## Trigger Systems

The trigger systems in ATLAS allows data to be recorded only when an event meets certain criteria. Without triggering there would be no way to decide which events to readout and which

to ignore. It would be impossible to readout every interaction that occurs in the detector. The reason for this is that the geometric constraints of the detector mean that there is only a small space available for readout wires, as detection medium needs to be prioritized for sensitivity and technology limits the data rate that one can achieve through a cable of fixed area. The trigger system comes in two parts, hardware component referred to as level one (L1) and software component referred to as the high level trigger (HLT). The L1 system is comprised of the L1 calorimeter (L1Calo) trigger which operates by searching for clusters of energy in the calorimeters and the L1 muon (L1Muon) system which coincidences in the muon systems. A third system L1 topological (L1Topo) uses regions of interest built from the L1Calo and L1Muon data which are passed to central trigger processors for selection. The various limitations of the hardware mean that these selections must be passed up to the next level of triggering, the HLT in a time window of  $2.5 \mu\text{s}$ . The HLT takes information from the L1 systems and uses faster versions of an offline style analysis in order to select or reject events for readout. Events must pass fully the trigger of one of the algorithms defined by an extensive trigger menu. More information about the triggers used in the  $VH(bb)$  analysis will be given in a later chapter.

# Chapter 4

## Analysis Strategy

This chapter gives a brief outline of the analysis strategy followed for a result shown at ICHEP 2018 [74] henceforth referred to as the ICHEP result. Due to similarities in the analysis procedures reference will also be made to the 2017 result published in JHEP [75] that will be referred to as the JHEP result.

### 4.1 Object reconstruction

Object reconstruction is largely the same for both the ICHEP and JHEP results.

As mentioned in Chapter 3 tracks in the inner detector are used to reconstruct interaction vertices, the method for this procedure is described in Ref. [76]. It was also previously mentioned that the interaction vertex associated with the highest energy hard scattering event is selected as primary however strictly speaking energy of a track is not measured. The actual procedure is to take the vertex with the highest sum of squared transverse momenta.

Electrons and muons are both reconstructed under a number of different criteria. These are referred to as loose or tight based on how stringent the requirements are for identification. For the electrons deposits of energy in the calorimeters must match a track in the ID, the parameters on which a loose or tight identification is made are the transverse momentum and pseudo-rapidity [77, 78]. For muons the procedure [79] is similar but instead of deposits of energy in the calorimeters the requirement is signatures in the muon spectrometers. Only tau particles which decay hadronically are reconstructed [80, 81] so that they are not identified as

jets.

The treatment of jets is complicated and only some of the details are given here. The algorithm used to reconstruct jets is the anti- $k_t$  algorithm [82], and a tool known as a jet vertex tagger [83] is used mitigate pollution from jets that come from secondary hard scatter vertices (known as pile-up vertices). The most obvious reason why jets are very important to this analysis is that the signature contains two b quarks. Given that all quarks initiate jets in the detector is important to have some way of identifying jets initiated by a b quark to those initiated by other flavours. The procedure used to achieve this is known as b-tagging with the MV2c10 multivariate discriminant [84] output value used a metric on which a threshold is decided above which a jet is considered b-tagged. Finally jets are calibrated using information on the jet energy scale [85, 86], a measure of how well the energy of a jet can be resolved in the detector.

Missing transverse energy is then calculated [87, 88] based on the known energy of the initial proton-proton collision and the summed up energy and momenta of the other reconstructed objects, this includes some objects not mentioned here.

## 4.2 Event Selection

The full event selection is different for all three channels considered in the analysis and can be found in Ref. [74]. Here a summary of some important details will be given. All channels require the presence of exactly two b-tagged jets in the event of which the leading b-tagged jet is required to have transverse momentum  $> 45$  GeV. All channels also require jet transverse momentum  $> 20$  GeV for  $|\eta| < 2.5$  and  $> 30$  GeV for  $2.5 < |\eta| < 4.5$ . The zero lepton channel uses missing transverse energy as a value on which to trigger as does the muon sub-channel of the one lepton channel whereas the electron sub-channel triggers using the single lepton trigger. Both of the one lepton sub-channels require a tight lepton of their respective flavours. Events for all channels may require exactly two jets, though for the zero and one lepton channels events with exactly three jets are also selected whereas in the two lepton channel any event with greater than three jets is also selected.

## 4.3 Multivariate analysis

Multivariate techniques are used to separate selected events into signal or background categories. There is also a version of the analysis based on making simple threshold cuts on variables however no details of that analysis will be given here. These algorithms are trained on simulated events which will be discussed briefly in the next section.

In total when all channels and variations of event selections are considered there are eight signal regions. These come from two and three jet selections in each of the three channels and additional two regions which will not be discussed. Boosted decision trees (BDTs) are used as the multivariate algorithm of choice and the final discriminating variables of the analysis are the outputs of these algorithms. Two different BDTs are trained one to perform the actual analysis and another to validate it. The analysis BDT is designed to separate Higgs boson events from all other backgrounds. The second BDT is used to classify so-called diboson events where a Z boson is produced in association with another vector boson of any type and then decays into two b quarks. Analysis of this process is chosen as a validation method due to the similarity yet orthogonality with the signal process. The ICHEP and JHEP results used the same BDT input variables with minor differences.

## 4.4 Data sets and simulation

A full table of the generators used to simulate signal and background processes can be found in Ref. [74]. Nothing more will be said here about the choice of these generators however it should be noted that the choice of tools used simulate events is tightly coupled with the results of the analysis. The performance of the BDTs discussed in the previous section can only be trusted if it can also be trusted that the simulated events that they were trained on match up as expected with events from real data.

## 4.5 Treatment of systematic uncertainties

The full treatment of systematic uncertainties can be found in Ref. [74], here only two systematics will be discussed as they relate to work completed by the author.

The decay of single top quarks in the  $Wt$ -channel is a background to the signal process in the one lepton channel. At next-to-leading order there exists an overlap between a  $Wt$  diagram and a  $t\bar{t}$  diagram [89] as shown in figure 4.1. This is a problem as decays of pairs of top quarks ( $t\bar{t}$ ) is also a background to the signal and so something needs to be done to stop the double counting of events. In order to counteract this problem two schemes are considered referred to as Diagram Removal and Diagram Subtraction, they are both discussed in Ref. [89]. The differences resulting from the use of the two schemes mentioned is the largest source of uncertainty on the single top systematic error.

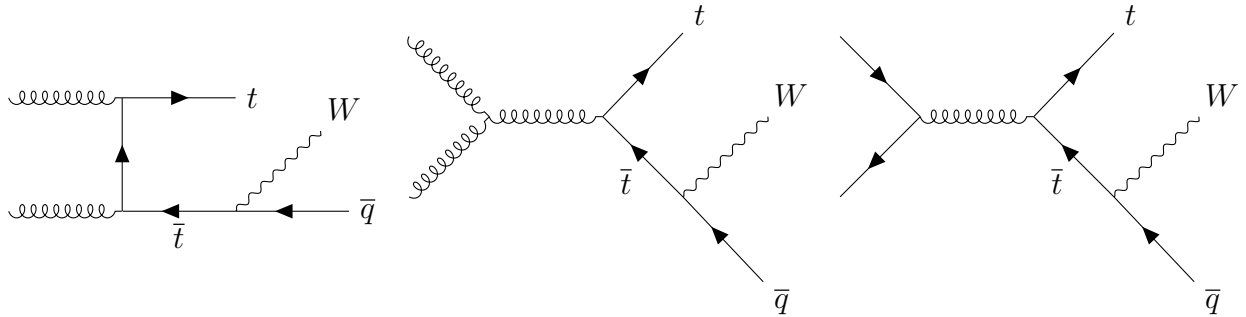


Figure 4.1: Leading order  $t\bar{t}$  diagrams that also contribute to  $Wt$  at next-to-leading order.

Currently this uncertainty is derived by analysing the normalisation, shapes and acceptance of the reconstructed di-jet mass  $m_{bb}$  and the transverse momentum of the vector boson. A potential improvement to these uncertainties is to use a bespoke BDT re-weighting algorithm to quantify the difference between the diagram removal and diagram subtraction samples in a higher dimensional phase space, results of a preliminary study into this technique will be shown in Chapter 5.

Another systematic uncertainty comes from diboson production, those events where any combination of gauge bosons are produced in association with one another. Events where  $WW$  only form a tiny fraction of the total background and so are not that important. The same

variables are used as in the single top procedure to look at normalisation, relative acceptance and shape in order to derive systematic uncertainties.

# Chapter 5

## Results

At ICHEP 2018 a result of the VH(bb) analysis was shown in which the Standard Model Higgs boson search at  $\sqrt{S} = 13$  TeV yielded an excess with an observed statistical significance of 4.9 standard deviations and a calculated expected significance of 4.3 standard deviations [74]. Further combining this result with the other Higgs production channels and results from Run 1 yielded an observed significance of 5.4 standard deviations with an expected significance of 5.5 standard deviations. This is above threshold for what is considered a discovery of the process.

### 5.1 Re-weighting of single top processes

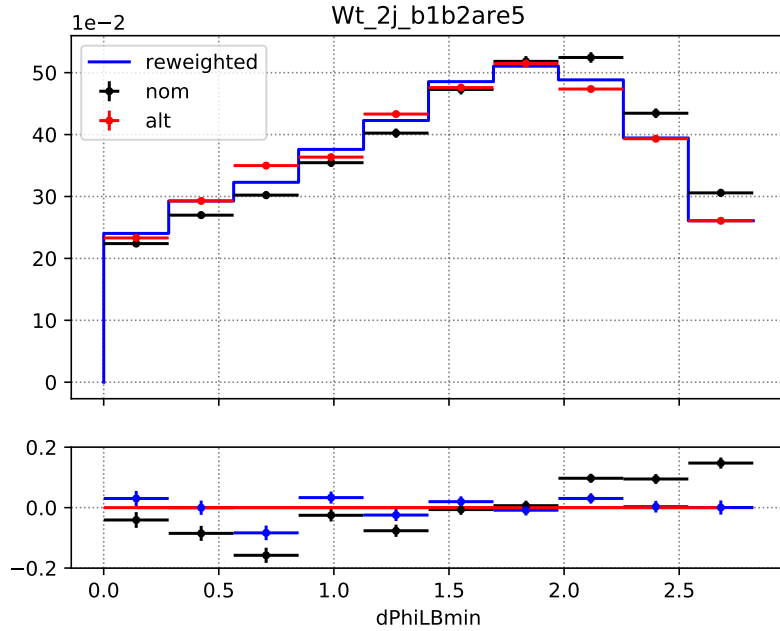
As mentioned in Chapter 4 a bespoke BDT re-weighting algorithm was studied to aim to quantify the difference between two generators of single top processes. The variables relevant to the  $Wt$  process are split up into four different subspaces which are each trained on separately. The spaces are defined as follows in table 5.1. Datasets used to train these algorithms are listed in Appendix A. The variables used for the training are shown in Appendix B. They differ for three jet and two jet samples but are unchanged by the number of b-jets. Two-fold cross validation was used to promote generalisation.

Figures 5.1, 5.2, 5.3, and 5.4 show one dimensional projects of some of the training variables. The distribution that was to be re-weighted is shown before (black) and after (blue) the weights are applied. A comparison can be made between the overall shape of these distributions and the target distribution (also plotted). It can be seen in these figures that, whilst performance varies

2 b-jets	$\leq 1$ b-jets	
subspace 2		
2 jets	subspace 1	
		subspace 4
3 jets	subspace 3	

Table 5.1: The four subspaces that events were split up into before training.

between variables, the BDT re-weighter consistently results in a shape that closely matches the target distribution. It should be noted that observing one dimensional projections does not give a complete comparison of the shapes of multi-dimensional distributions. It is also noted that more work needs to be completed before these results can be turned into a proper systematic uncertainty.

Figure 5.1: Plot of  $\min(\Delta\phi(\ell, \text{jet}))$  in the sub-space where there are two jets that are both b-jets.

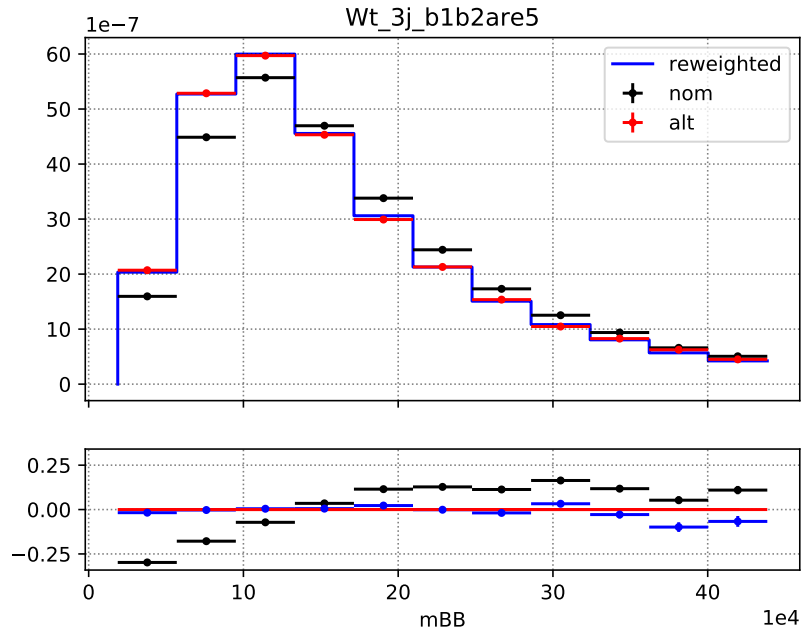


Figure 5.2: Plot of  $m_{jj}$  in the sub-space where there are three jets and exactly two are b-jets.

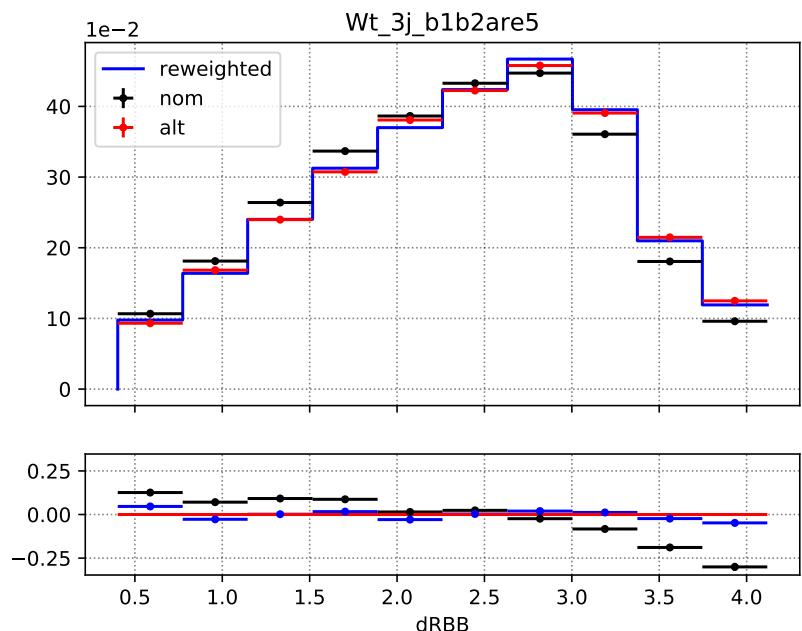


Figure 5.3: Plot of  $\Delta R(jet_1, jet_2)$  in the sub-space where there are three jets and exactly two are b-jets.

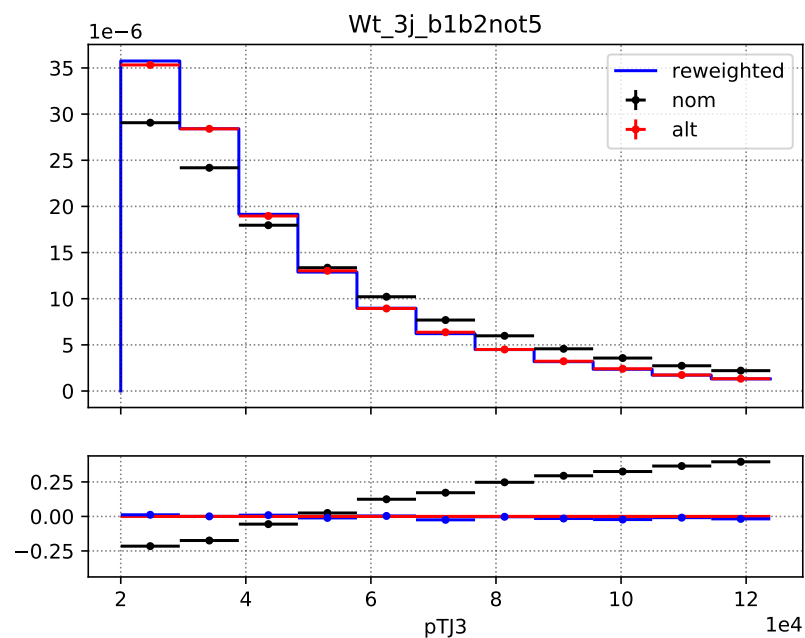


Figure 5.4: Plot of  $p_T^{jet3}$  in the sub-space where there are three jets of which, the leading and sub-leading jets are not both b-jets (one is allowed).

# Chapter 6

## Conclusion and improvements

A summary of the sub detectors that make up the ATLAS detector at the LHC has been given and referred to throughout the detailing of the Higgs boson analysis in which the Higgs is produced in association with a vector boson and decays into two b quarks. The relevant physics theory was described and the Brout-Englert-Higgs mechanism was described in basic detail in order to motivate the importance of Higgs boson measurements. The analysis strategy has been described in some detail with references to the full procedures provided. The main stages of the analysis are as follows. Object reconstruction, which relies heavily on the tools and studies carried about the ATLAS collaboration. Event selection which is motivated by the physics theory that underlies the entire analysis. The multivariate analysis which takes the outputs of the object reconstruction and event selection and uses powerful statistical techniques to exploit as much information that these variables contain as possible in forming a discriminant on the signal and background. The treatment of statistical uncertainties, which is crucial to bring the result into the real world by accounting for limitations of the detector and theoretical techniques used to generate simulations. Overall when everything is taken into consideration the observed significance of the signal process was over 5 standard deviations, the threshold for a discovery.

One way that an improvement might be made to the analysis has been discussed. The use of a new bespoke algorithm to perform high dimensional re-weighting could be used in order to quantify systematic uncertainties. Similarly studies will be performed in the future to determine if any advancements in machine learning (a rapidly growing field of research in itself) can be

used in order to improve any of the areas where multivariate techniques are used, namely the classification BDT used in the main analysis and in the b-tagging algorithms used in event selection.

# Bibliography

- [1] D. de Florian et al. Handbook of LHC Higgs Cross Sections: 4. Deciphering the Nature of the Higgs Sector. 2016. doi: 10.23731/CYRM-2017-002.
- [2] Christiane Lefèvre. The CERN accelerator complex. Complexe des accélérateurs du CERN. Dec 2008. URL <https://cds.cern.ch/record/1260465>.
- [3] Joao Pequenao. Computer generated image of the whole ATLAS detector. Mar 2008. URL <https://cds.cern.ch/record/1095924>.
- [4] H.H.J. ten Kate. The atlas superconducting magnet system at the large hadron collider. *Physica C: Superconductivity*, 468(15):2137 – 2142, 2008. ISSN 0921-4534. doi: <https://doi.org/10.1016/j.physc.2008.05.146>. URL <http://www.sciencedirect.com/science/article/pii/S0921453408004541>. Proceedings of the 20th International Symposium on Superconductivity (ISS 2007).
- [5] Joao Pequenao. Computer generated image of the ATLAS inner detector. Mar 2008. URL <https://cds.cern.ch/record/1095926>.
- [6] Thomas Paul Charman, Bart Hommels, and Adrian John Bevan. Authorship Qualification Task: ATLAS ITk Sensor Scanner Documentation (QMUL). Technical Report ATL-COM-ITK-2019-018, CERN, Geneva, Jan 2019. URL <https://cds.cern.ch/record/2674404>.
- [7] Ben Brueers. The design and layout of the Phase-II upgrade of the Inner tracker of the ATLAS experiment. Jul 2019. URL <https://cds.cern.ch/record/2681301>.
- [8] John Stakely Keller. The ATLAS ITk Strip Detector System for the Phase-II LHC Upgrade. Feb 2019. URL <https://cds.cern.ch/record/2663172>.

- [9] Joao Pequenao. Computer Generated image of the ATLAS calorimeter. Mar 2008. URL <https://cds.cern.ch/record/1095927>.
- [10] Joao Pequenao. Computer generated image of the ATLAS Muons subsystem. Mar 2008. URL <https://cds.cern.ch/record/1095929>.
- [11] Georges Aad et al. (ATLAS Collaboration). Observation of a new particle in the search for the Standard Model Higgs boson with the ATLAS detector at the LHC. *Phys. Lett.*, B716:1–29, 2012. doi: 10.1016/j.physletb.2012.08.020.
- [12] Serguei Chatrchyan et al. (CMS Collaboration). Observation of a new boson at a mass of 125 GeV with the CMS experiment at the LHC. *Phys. Lett.*, B716:30–61, 2012. doi: 10.1016/j.physletb.2012.08.021.
- [13] Will J. Percival, Shaun Cole, Daniel J. Eisenstein, Robert C. Nichol, John A. Peacock, Adrian C. Pope, and Alexander S. Szalay. Measuring the baryon acoustic oscillation scale using the Sloan Digital Sky Survey and 2dF Galaxy Redshift Survey. *Monthly Notices of the Royal Astronomical Society*, 381(3):1053–1066, 2007. doi: 10.1111/j.1365-2966.2007.12268.x. URL <http://dx.doi.org/10.1111/j.1365-2966.2007.12268.x>.
- [14] Fabio Iocco, Gianpiero Mangano, Gennaro Miele, Ofelia Pisanti, and Pasquale D. Serpico. Primordial Nucleosynthesis: from precision cosmology to fundamental physics. *Phys. Rept.*, 472:1–76, 2009. doi: 10.1016/j.physrep.2009.02.002.
- [15] M. Kowalski et al. Improved Cosmological Constraints from New, Old and Combined Supernova Datasets. *Astrophys. J.*, 686:749–778, 2008. doi: 10.1086/589937.
- [16] Richard Massey et al. Dark matter maps reveal cosmic scaffolding. *Nature*, 445:286, 2007. doi: 10.1038/nature05497.
- [17] Douglas Clowe, Marusa Bradac, Anthony H. Gonzalez, Maxim Markevitch, Scott W. Randall, Christine Jones, and Dennis Zaritsky. A direct empirical proof of the existence of dark matter. *Astrophys. J.*, 648:L109–L113, 2006. doi: 10.1086/508162.

- [18] J. Anthony Tyson, Greg P. Kochanski, and Ian P. Dell'Antonio. Detailed mass map of CL0024+1654 from strong lensing. *Astrophys. J.*, 498:L107, 1998. doi: 10.1086/311314.
- [19] Lars Bergstrom. Dark Matter Candidates. *New J. Phys.*, 11:105006, 2009. doi: 10.1088/1367-2630/11/10/105006.
- [20] C. Patrignani et al. Review of Particle Physics. *Chin. Phys.*, C40(10):100001, 2016. doi: 10.1088/1674-1137/40/10/100001.
- [21] F. Zwicky. Republication of: The redshift of extragalactic nebulae. *General Relativity and Gravitation*, 41:207–224, January 2009. doi: 10.1007/s10714-008-0707-4.
- [22] Lars Bergström. Nonbaryonic dark matter: Observational evidence and detection methods. *Rept. Prog. Phys.*, 63:793, 2000. doi: 10.1088/0034-4885/63/5/2r3.
- [23] Gianfranco Bertone, Dan Hooper, and Joseph Silk. Particle dark matter: Evidence, candidates and constraints. *Phys. Rept.*, 405:279–390, 2005. doi: 10.1016/j.physrep.2004.08.031.
- [24] Roel Aaij et al. Measurement of the ratio of branching fractions  $\mathcal{B}(\bar{B}^0 \rightarrow D^{*+}\tau^-\bar{\nu}_\tau)/\mathcal{B}(\bar{B}^0 \rightarrow D^{*+}\mu^-\bar{\nu}_\mu)$ . *Phys. Rev. Lett.*, 115(11):111803, 2015. doi: 10.1103/PhysRevLett.115.159901, 10.1103/PhysRevLett.115.111803. [Erratum: *Phys. Rev. Lett.* 115,no.15,159901(2015)].
- [25] J. P. Lees et al. Evidence for an excess of  $\bar{B} \rightarrow D^{(*)}\tau^-\bar{\nu}_\tau$  decays. *Phys. Rev. Lett.*, 109:101802, 2012. doi: 10.1103/PhysRevLett.109.101802.
- [26] Thomas Blum, Achim Denig, Ivan Logashenko, Eduardo de Rafael, B. Lee Roberts, Thomas Teubner, and Graziano Venanzoni. The Muon (g-2) Theory Value: Present and Future. 2013.
- [27] Carl E. Carlson. The Proton Radius Puzzle. *Prog. Part. Nucl. Phys.*, 82:59–77, 2015. doi: 10.1016/j.ppnp.2015.01.002.
- [28] Bernat Capdevila, Andreas Crivellin, Sébastien Descotes-Genon, Joaquim Matias, and Javier Virto. Patterns of New Physics in  $b \rightarrow s\ell^+\ell^-$  transitions in the light of recent data. *JHEP*, 01:093, 2018. doi: 10.1007/JHEP01(2018)093.

- [29] John D. Hobbs, Mark S. Neubauer, and Scott Willenbrock. Tests of the standard electroweak model at the energy frontier. *Rev. Mod. Phys.*, 84:1477–1526, Oct 2012. doi: 10.1103/RevModPhys.84.1477. URL <https://link.aps.org/doi/10.1103/RevModPhys.84.1477>.
- [30] L. Nodulman. Experimental tests of the standard model. *NATO Sci. Ser. C*, 534:147–193, 1999. doi: 10.1007/978-94-011-4689-0\_4.
- [31] Morad Aaboud et al. Observation of  $H \rightarrow b\bar{b}$  decays and  $VH$  production with the ATLAS detector. *Phys. Lett.*, B786:59–86, 2018. doi: 10.1016/j.physletb.2018.09.013.
- [32] Francis Halzen, Alan D. Martin, and Nilotpal Mitra. Quarks and leptons: An introductory course in modern particle physics. *American Journal of Physics*, 53(3):287–287, 1985. doi: 10.1119/1.14146. URL <https://doi.org/10.1119/1.14146>.
- [33] Mark Thomson. *Modern Particle Physics*. Cambridge University Press, 2013. doi: 10.1017/CBO9781139525367.
- [34] A. Zannoni. On the Quantization of the Monoatomic Ideal Gas. *eprint arXiv:cond-mat/9912229*, December 1999.
- [35] On the theory of quantum mechanics. *Proceedings of the Royal Society of London A: Mathematical, Physical and Engineering Sciences*, 112(762):661–677, 1926. ISSN 0950-1207. doi: 10.1098/rspa.1926.0133. URL <http://rspa.royalsocietypublishing.org/content/112/762/661>.
- [36] A. Borrelli. *Compendium of Quantum Physics*. 2009.
- [37] Albert Einstein. On the electrodynamics of moving bodies. *Annalen Phys.*, 17:891–921, 1905. doi: 10.1002/andp.200590006. [Annalen Phys.14,194(2005)].
- [38] V. Alan Kostelecký and Neil Russell. Data tables for lorentz and *cpt* violation. *Rev. Mod. Phys.*, 83:11–31, Mar 2011. doi: 10.1103/RevModPhys.83.11. URL <https://link.aps.org/doi/10.1103/RevModPhys.83.11>.

- [39] David Mattingly. Modern tests of lorentz invariance. *Living Reviews in Relativity*, 8(1):5, Sep 2005. ISSN 1433-8351. doi: 10.12942/lrr-2005-5. URL <https://doi.org/10.12942/lrr-2005-5>.
- [40] S Liberati. Tests of lorentz invariance: a 2013 update. *Classical and Quantum Gravity*, 30(13):133001, jun 2013. doi: 10.1088/0264-9381/30/13/133001. URL <https://doi.org/10.1088%2F0264-9381%2F30%2F13%2F133001>.
- [41] Clifford M. Will Mark P. Haugan. Modern tests of special relativity. *Physics Today*, 40(5):69, 1987. doi: 10.1063/1.881074. URL <https://doi.org/10.1063/1.881074>.
- [42] Floyd W. Stecker. Limiting superluminal electron and neutrino velocities using the 2010 crab nebula flare and the icecube pev neutrino events. *Astroparticle Physics*, 56:16 – 18, 2014. ISSN 0927-6505. doi: <https://doi.org/10.1016/j.astropartphys.2014.02.007>. URL <http://www.sciencedirect.com/science/article/pii/S092765051400019X>.
- [43] R. Abbasi et al. Search for a lorentz-violating sidereal signal with atmospheric neutrinos in icecube. *Phys. Rev. D*, 82:112003, Dec 2010. doi: 10.1103/PhysRevD.82.112003. URL <https://link.aps.org/doi/10.1103/PhysRevD.82.112003>.
- [44] Enrico Borriello, Sovan Chakraborty, Alessandro Mirizzi, and Pasquale Dario Serpico. Stringent constraint on neutrino lorentz invariance violation from the two icecube pev neutrinos. *Phys. Rev. D*, 87:116009, Jun 2013. doi: 10.1103/PhysRevD.87.116009. URL <https://link.aps.org/doi/10.1103/PhysRevD.87.116009>.
- [45] E. Schrödinger. An undulatory theory of the mechanics of atoms and molecules. *Phys. Rev.*, 28:1049–1070, Dec 1926. doi: 10.1103/PhysRev.28.1049. URL <https://link.aps.org/doi/10.1103/PhysRev.28.1049>.
- [46] Sheldon L. Glashow. The renormalizability of vector meson interactions. *Nucl. Phys.*, 10:107–117, 1959. doi: 10.1016/0029-5582(59)90196-8.
- [47] Abdus Salam and John Clive Ward. Weak and electromagnetic interactions. *Nuovo Cim.*, 11:568–577, 1959. doi: 10.1007/BF02726525.

- [48] Steven Weinberg. A Model of Leptons. *Phys. Rev. Lett.*, 19:1264–1266, 1967. doi: 10.1103/PhysRevLett.19.1264.
- [49] C. S. Wu, E. Ambler, R. W. Hayward, D. D. Hoppes, and R. P. Hudson. Experimental test of parity conservation in beta decay. *Phys. Rev.*, 105:1413–1415, Feb 1957. doi: 10.1103/PhysRev.105.1413. URL <https://link.aps.org/doi/10.1103/PhysRev.105.1413>.
- [50] G. Arnison et al. Experimental Observation of Isolated Large Transverse Energy Electrons with Associated Missing Energy at  $s^{**}(1/2) = 540\text{-GeV}$ . *Phys. Lett.*, B122:103–116, 1983. doi: 10.1016/0370-2693(83)91177-2. [,611(1983)].
- [51] M. Banner et al. Observation of Single Isolated Electrons of High Transverse Momentum in Events with Missing Transverse Energy at the CERN anti-p p Collider. *Phys. Lett.*, B122:476–485, 1983. doi: 10.1016/0370-2693(83)91605-2. [,7.45(1983)].
- [52] G. Arnison et al. Experimental Observation of Lepton Pairs of Invariant Mass Around 95- $\text{GeV}/c^{**2}$  at the CERN SPS Collider. *Phys. Lett.*, B126:398–410, 1983. doi: 10.1016/0370-2693(83)90188-0. [,7.55(1983)].
- [53] P. Bagnaia et al. Evidence for  $Z_0 \rightarrow e^+ e^-$  at the CERN anti-p p Collider. *Phys. Lett.*, B129:130–140, 1983. doi: 10.1016/0370-2693(83)90744-X. [,7.69(1983)].
- [54] F. Englert and R. Brout. Broken symmetry and the mass of gauge vector mesons. *Phys. Rev. Lett.*, 13:321–323, Aug 1964. doi: 10.1103/PhysRevLett.13.321. URL <https://link.aps.org/doi/10.1103/PhysRevLett.13.321>.
- [55] Peter W. Higgs. Broken symmetries and the masses of gauge bosons. *Phys. Rev. Lett.*, 13:508–509, Oct 1964. doi: 10.1103/PhysRevLett.13.508. URL <https://link.aps.org/doi/10.1103/PhysRevLett.13.508>.
- [56] G. S. Guralnik, C. R. Hagen, and T. W. B. Kibble. Global conservation laws and massless particles. *Phys. Rev. Lett.*, 13:585–587, Nov 1964. doi: 10.1103/PhysRevLett.13.585. URL <https://link.aps.org/doi/10.1103/PhysRevLett.13.585>.

- [57] P. W. Anderson. Plasmons, gauge invariance, and mass. *Phys. Rev.*, 130:439–442, Apr 1963. doi: 10.1103/PhysRev.130.439. URL <https://link.aps.org/doi/10.1103/PhysRev.130.439>.
- [58] Oliver Sim Brüning, Paul Collier, P Lebrun, Stephen Myers, Ranko Ostojic, John Poole, and Paul Proudlock. *LHC Design Report*. CERN Yellow Reports: Monographs. CERN, Geneva, 2004. URL <https://cds.cern.ch/record/782076>.
- [59] *LEP design report*. CERN, Geneva, 1984. URL <https://cds.cern.ch/record/102083>. Copies shelved as reports in LEP, PS and SPS libraries.
- [60] CERN. ATLAS: Letter of intent for a general purpose p p experiment at the large hadron collider at CERN. 1992.
- [61] M. Della Negra et al. CMS: letter of intent by the CMS Collaboration for a general purpose detector at LHC. Technical Report CERN-LHCC-92-003. LHCC-I-1, CERN, Geneva, 1992. URL <https://cds.cern.ch/record/290808>. Open presentation to the LHCC 5 November 1992, M. Della Negra/CERN, CMS Spokesman.
- [62] H. Dijkstra, Hans Jürgen Hilke, Tatsuya Nakada, and Thomas Ypsilantis. LHCb Letter of Intent, LHCb Collaboration. 1995.
- [63] Letter of Intent for A Large Ion Collider Experiment [ALICE]. Technical Report CERN-LHCC-93-016. LHCC-I-4, CERN, Geneva, 1993. URL <https://cds.cern.ch/record/290825>.
- [64] G Giacomelli, A A Faust, and James L Pinfold. A search for highly ionizing particles and slow exotic decays at the LHC using the MOEDAL detectors: letter of intent. Technical Report CERN-LHCC-98-05. LHCC-I-19, CERN, Geneva, Feb 1998. URL <https://cds.cern.ch/record/347906>.
- [65] W Kienzle, , et al. *Total cross section: elastic scattering and diffraction dissociation at the LHC*. Letter of Intent. CERN, Geneva, 1997. URL <http://cds.cern.ch/record/335255>.

- [66] O Adriani. LHCf Letter of Intent for a p-Pb run. A precise study of forward physics in  $\sqrt{s_{NN}} = 4.4$  TeV proton-Lead ion collisions with LHCf at the LHC. Technical Report CERN-LHCC-2011-015. LHCC-I-021, CERN, Geneva, Dec 2011. URL <https://cds.cern.ch/record/1404163>.
- [67] Roel Aaij et al. Observation of CP Violation in Charm Decays. *Phys. Rev. Lett.*, 122(21):211803, 2019. doi: 10.1103/PhysRevLett.122.211803.
- [68] I. Bejar Alonso and L. Rossi. HiLumi LHC Technical Design Report. 2015.
- [69] Georges Aad et al. (ATLAS Collaboration). The atlas experiment at the cern large hadron collider. *Journal of Instrumentation*, 3(08):S08003, 2008. URL <http://stacks.iop.org/1748-0221/3/i=08/a=S08003>.
- [70] David Hanser. *Architecture of France*. Greenwood Press, Westport, Conn, 2006. ISBN 978-0-313-31902-0.
- [71] A. Airapetian et al. ATLAS: Detector and physics performance technical design report. Volume 1. 1999.
- [72] A. Airapetian et al. ATLAS: Detector and physics performance technical design report. Volume 2. 1999.
- [73] M Capeans, G Darbo, K Einsweiller, M Elsing, T Flick, M Garcia-Sciveres, C Gemme, H Pernegger, O Rohne, and R Vuillermet. ATLAS Insertable B-Layer Technical Design Report. Technical Report CERN-LHCC-2010-013. ATLAS-TDR-19, Sep 2010. URL <https://cds.cern.ch/record/1291633>.
- [74] Observation of  $H \rightarrow b\bar{b}$  decays and  $VH$  production with the ATLAS detector. Technical Report ATLAS-CONF-2018-036, CERN, Geneva, Jul 2018. URL <https://cds.cern.ch/record/2630338>.
- [75] M. Aaboud et al. Evidence for the  $H \rightarrow b\bar{b}$  decay with the ATLAS detector. *JHEP*, 12:024, 2017. doi: 10.1007/JHEP12(2017)024.

- [76] Morad Aaboud et al. Reconstruction of primary vertices at the ATLAS experiment in Run 1 proton–proton collisions at the LHC. *Eur. Phys. J.*, C77(5):332, 2017. doi: 10.1140/epjc/s10052-017-4887-5.
- [77] Electron efficiency measurements with the ATLAS detector using the 2015 LHC proton–proton collision data. Technical Report ATLAS-CONF-2016-024, CERN, Geneva, Jun 2016. URL <https://cds.cern.ch/record/2157687>.
- [78] Morad Aaboud et al. Electron efficiency measurements with the ATLAS detector using 2012 LHC proton–proton collision data. *Eur. Phys. J.*, C77(3):195, 2017. doi: 10.1140/epjc/s10052-017-4756-2.
- [79] Georges Aad et al. Muon reconstruction performance of the ATLAS detector in proton–proton collision data at  $\sqrt{s} = 13$  TeV. *Eur. Phys. J.*, C76(5):292, 2016. doi: 10.1140/epjc/s10052-016-4120-y.
- [80] Georges Aad et al. Reconstruction of hadronic decay products of tau leptons with the ATLAS experiment. *Eur. Phys. J.*, C76(5):295, 2016. doi: 10.1140/epjc/s10052-016-4110-0.
- [81] Measurement of the tau lepton reconstruction and identification performance in the ATLAS experiment using  $pp$  collisions at  $\sqrt{s} = 13$  TeV. Technical Report ATLAS-CONF-2017-029, CERN, Geneva, May 2017. URL <https://cds.cern.ch/record/2261772>.
- [82] Matteo Cacciari, Gavin P. Salam, and Gregory Soyez. The Anti- $k(t)$  jet clustering algorithm. *JHEP*, 04:063, 2008. doi: 10.1088/1126-6708/2008/04/063.
- [83] Georges Aad et al. Performance of pile-up mitigation techniques for jets in  $pp$  collisions at  $\sqrt{s} = 8$  TeV using the ATLAS detector. *Eur. Phys. J.*, C76(11):581, 2016. doi: 10.1140/epjc/s10052-016-4395-z.
- [84] Optimisation and performance studies of the ATLAS  $b$ -tagging algorithms for the 2017-18 LHC run. Technical Report ATL-PHYS-PUB-2017-013, CERN, Geneva, Jul 2017. URL <https://cds.cern.ch/record/2273281>.

- [85] Georges Aad et al. Jet energy measurement and its systematic uncertainty in proton-proton collisions at  $\sqrt{s} = 7$  TeV with the ATLAS detector. *Eur. Phys. J.*, C75:17, 2015. doi: 10.1140/epjc/s10052-014-3190-y.
- [86] M. Aaboud et al. Jet energy scale measurements and their systematic uncertainties in proton-proton collisions at  $\sqrt{s} = 13$  TeV with the ATLAS detector. *Phys. Rev.*, D96(7):072002, 2017. doi: 10.1103/PhysRevD.96.072002.
- [87] Expected performance of missing transverse momentum reconstruction for the ATLAS detector at  $\sqrt{s} = 13$  TeV. Technical Report ATL-PHYS-PUB-2015-023, CERN, Geneva, Jul 2015. URL <https://cds.cern.ch/record/2037700>.
- [88] Performance of missing transverse momentum reconstruction for the ATLAS detector in the first proton-proton collisions at  $\sqrt{s} = 13$  TeV. Technical Report ATL-PHYS-PUB-2015-027, CERN, Geneva, Jul 2015. URL <https://cds.cern.ch/record/2037904>.
- [89] Chris D. White, Stefano Frixione, Eric Laenen, and Fabio Maltoni. Isolating wt production at the lhc. *Journal of High Energy Physics*, 2009(11):074, 2009. URL <http://stacks.iop.org/1126-6708/2009/i=11/a=074>.

# Appendix A

## Datasets

Name	DS ID	Process	Events
Nominal	410013	Single top $Wt$ incl $t$	4985800
Nominal	410014	Single top $Wt$ incl $\bar{t}$	4985600
Alternative	410062	Single top DS $Wt$ incl $t$	4948600
Alternative	410063	Single top DS $Wt$ incl $\bar{t}$	4983000

Table A.1: Datasets used to train the BDT re-weighting algorithm.

# Appendix B

## Full Features List

Variable	2 jet	3 jet
$\min(\Delta\phi(\ell, jet))$	✓	✓
$\Delta\phi(V, H)$	✓	✓
$\Delta R(jet_1, jet_2)$	✓	✓
$\Delta Y(W, H)$	✓	✓
$m_{jj}$	✓	✓
$m_{jjj}$		✓
$E_T^{miss}$	✓	✓
$m_{top}$	✓	✓
$m_T^W$	✓	✓
$p_T^{jet1}$	✓	✓
$p_T^{jet2}$	✓	✓
$p_T^{jet3}$		✓
$p_T^V$	✓	✓

Table B.1: Training variables for samples containing 2 and 3 jets.

# Appendix C

## Theory Supplement

### C.1 Symmetries

Gauge group  $SU(3)_c \times SU(2)_L \times U(1)_Y$

Global Abelian U (1) transformation

$$\phi(x) \rightarrow \phi'(x) = e^{i\alpha} \phi(x) \quad (\text{C.1})$$

Considering Lagrangian:

$$\mathcal{L} = \partial_\mu \phi^* \partial_\mu \phi - m^2 \phi^* \phi - \frac{\lambda}{2} (\phi^* \phi)^2, \quad (\text{C.2})$$

which is invariant under C.1, we can think about the consequences of this symmetry. Given that complex conjugation is applied to the field  $\phi$  it is implicit that this field can be expanded as  $\phi = \frac{1}{\sqrt{2}}(\phi_1 + i\phi_2)$  then the middle term of C.2 can be expanded as

$$m^2 \phi^* \phi = \frac{m^2}{2} (\phi_1^2 + \phi_2^2) \quad (\text{C.3})$$

which implies by comparison with the mass term in the real Klein-Gordon equation that  $\phi_1$  and  $\phi_2$  have equal mass.

## C.2 Gauge Bosons and the Higgs

Starting with a complex doublet

$$\Phi = \begin{pmatrix} \phi_1 \\ \phi_2 \end{pmatrix}, \quad (\text{C.4})$$

the Lagrangian invariant under the required symmetry is

$$\mathcal{L} = -\frac{1}{4}F_{\mu\nu}^a F^{a\mu\nu} - \frac{1}{4}B_{\mu\nu}B^{\mu\nu} + (D_\mu\Phi)^\dagger D_\mu\Phi - \lambda \left( \Phi^\dagger\Phi - \frac{v^2}{2} \right)^2, \quad (\text{C.5})$$

with

$$F_{\mu\nu}^a = \partial_\mu A_\nu^a - \partial_\nu A_\mu^a + g\epsilon^{abc}A_\mu^b A_\nu^c, \quad (\text{C.6})$$

$$B_{\mu\nu} = \partial_\mu B_\nu - \partial_\nu B_\mu, \quad (\text{C.7})$$

and

$$D_\mu\Phi = \partial_\mu\Phi - i\frac{g}{2}\tau^a A_\mu^a (hi - i\frac{g'}{2}B_\mu\Phi) \quad (\text{C.8})$$

## C.3 SM Lagrangian before and after spontaneous symmetry breaking

Before spontaneous symmetry breaking:

$$\mathcal{L} = -\frac{1}{2}\text{Tr}[G_{\mu\nu}G^{\mu\nu}] - \frac{1}{2}\text{Tr}[W_{\mu\nu}W^{\mu\nu}] - \frac{1}{2}\text{Tr}[B_{\mu\nu}B^{\mu\nu}] \quad (\text{C.9})$$

$$+ \sum_\psi i\bar{\psi}\not{D}\psi + \sum_{f,g} -G_e^{fg}\bar{\chi}_L^f\Phi e_R^g - G_D^{fg}\bar{Q}_L^f\Phi D_R^g - G_U^{fg}\bar{Q}_L^f\Phi^c U_R^g \quad (\text{C.10})$$

$$+ (D_\mu\Phi)^\dagger D_\mu\Phi - \lambda \left( \Phi^\dagger\Phi - \frac{v^2}{2} \right)^2 \quad (\text{C.11})$$

where  $\psi = \chi_L, e_r, Q_L, U_R, D_R$  in the sum.

After spontaneous symmetry breaking:

$$\mathcal{L} = \mathcal{L}_{QCD} + \mathcal{L}_{lept} + \mathcal{L}_{f,EM} + \mathcal{L}_{f,weak} + \mathcal{L}_Y + \mathcal{L}_V + \mathcal{L}_H + \mathcal{L}_{VH} \quad (\text{C.12})$$

with:

$$\mathcal{L}_{QCD} = -\frac{1}{4}G_{\mu\nu}^a G^{a\mu\nu} + \sum_{quarks} \bar{q}(i\cancel{\partial} - m_q - g_s \frac{\lambda^a}{2} G^a) q,$$

$$\mathcal{L}_{lept} = \sum_{g=e,\mu,\tau} \bar{e}_g(i\cancel{\partial} - m_{e_g}) e_g + \sum_g \bar{\nu}_g i\cancel{\partial} P_L \nu_g,$$

$$\mathcal{L}_{f,EM} = e A_\mu \sum_f Q_f \bar{f} \gamma^\mu f,$$

$$\mathcal{L}_{f,weak} = \frac{g}{2\sqrt{2}} W_\mu \sum_g \bar{\nu}_g \gamma^\mu P_L e_g + h.c.$$

$$+ \frac{g}{2\sqrt{2}} W_\mu \sum_{f,g} \bar{u}_f \gamma^\mu P_L V_{fg} d_g + h.c.$$

$$+ \frac{g}{2 \cos \theta_W} Z_\mu \sum_{fermions} \bar{f} \gamma^\mu (T_3^f P_L - 2 Q_f \sin^2 \theta_W) f,$$

$$\mathcal{L}_Y =$$

$$\mathcal{L}_V =$$

$$\mathcal{L}_H =$$

$$\mathcal{L}_{VH} =$$

